3-D complex resistivity imaging using controlled source electromagnetic data: a multistage procedure using a second order polynomial parametrization

J Porté, François Bretaudeau, J F Girard

Geophysical Journal International

Geophys. J. Int. (2023) **233,** 839–860
Advance Access publication 2022 December 09
GJI Marine Geosciences and Applied Geophysics

https://doi.org/10.1093/gji/ggac486

3-D complex resistivity imaging using controlled source electromagnetic data: a multistage procedure using a second order polynomial parametrization

J. Porté [1,2,*] F. Bretaudeau [2] and J.F. Girard [1]

[1] *University of Strasbourg, CNRS, Géophysique Expérimentale, ITES - UMR* 7063, *F*-67000 *Strasbourg, France. E-mail: j.porte210@gmail.com*
[2] *French Geological Survey, BRGM, DRP-IGT*. *adv. Petroleum, F*-45100 *Orléans, France*

Accepted 2022 December 7. Received 2022 November 22; in original form 2021 December 7

SUMMARY

In some Earth materials, significant induced polarization (IP) phenomena are occurring when an electric perturbation is applied. These mechanisms are described by a frequency-dependent complex resistivity (CR). The study of the CR spectral signature allows to access indirectly to several properties of interest of the subsurface linked to the interaction between the pore space and fluids. CR is usually studied using the electrical method with a direct current approximation, neglecting by the way electromagnetic (EM) induction that can occur in the data. However, EM induction increases with frequency and offset, resulting in limitations at high frequencies or for the investigation of deep target. We implemented a frequency-dependent CR in a 3-D finite-differences (FD) modelling and inversion code for frequency domain controlled-source electromagnetic (CSEM) data to take into consideration IP information contained in EM data or reciprocally. The CSEM methods are resistivity imaging techniques using multifrequency EM fields that fully take into account EM induction with large investigation depth. Following a preliminary sensitivity study, a multistage inversion framework was designed to constrain the multiparameter inverse problem. Furthermore, to manage the increasing number of parameters, a second-order polynomial parametrization is used to describe independently frequency variation of CR norm and phase. We demonstrate the method through 1-D and 3-D synthetic data inversions for a deep-target model. We show that we were able to recover the CR and its frequency variation from CSEM data in the IP/EM coupling domain for 1-D targets. The problem of deep polarizable 3-D targets is more challenging and the resolution of the recovered CR spectrum was impacted. Nevertheless, we retrieved from a model containing several polarizable anomalies some crucial information allowing the discrimination of the targets from the non-polarizable background and from different spectral CR signatures. Our inversion strategy allows thus accessing to IP parameters of the medium in an extended frequency domain by fully taking EM induction information into account.

Key words: Electrical properties; Controlled source electromagnetics (CSEM); Inverse theory.

1 INTRODUCTION

Electric resistivity of Earth materials varies over many magnitudes depending on the type of rocks (Palacky 1988) and is linked to various physico-chemical properties of the medium as resistivity is mainly sensitive to fluids. Its wide range of variation makes resistivity imaging a privileged way to access to medium properties such as porosity, salinity (Archie 1942), clay content (Waxman & Smits 1968) or mineralization. Resistivity imaging using electric prospecting relies on the measurement of the potential difference measured between two receiver electrodes due to the injection of a direct current (DC) between two transmitter electrodes at different offsets. The ground apparent resistivity is deduced for different electrode configurations using a geometrical coefficient. The resistivity is usually considered as a constant and real parameter in many geophysical applications.

Nevertheless, overvoltage phenomena or induced polarization (IP), can occur in the ground due to its chargeability (Seigel 1959). Chargeability of the ground results from the relaxation phenomenon occurring after the current cut-off with a slow voltage decay that cannot be attributed to electromagnetic (EM) induction. IP effects

*Now at: SINTEF Industry, 7031 Trondheim, Norway

are due to the transport and reversible accumulation of charges between grain and fluid interfaces when perturbed by an external electric field. In an overview of the spectral induced polarization (SIP) method (Kemna *et al.* 2012) summarized four kinds of polarization mechanisms responsible of IP: Maxwell–Wagner effect, polarization of the electric double layer (EDL), membrane polarization and electrode polarization.

To model these effects, the electric resistivity ρ^* is expressed as a complex and frequency dependent parameter:

$$\rho^*(\omega) = \rho_r(\omega) + i\rho_q(\omega), \tag{1}$$

with ρ_r and ρ_q the real and the imaginary part of the resistivity, respectively, with $\rho_q \ll \rho_r$. ω is the angular frequency and i the imaginary number $i = \sqrt{-1}$. Its exponential form can also be used:

$$\rho^*(\omega) = |\rho^*(\omega)|e^{i\phi_{\text{cpx}}(\omega)}$$
$$\text{with} \quad \begin{cases} |\rho^*(\omega)| = \sqrt{\rho_r^2(\omega) + \rho_q^2(\omega)} \\ \phi_{\text{cpx}}(\omega) = \arctan\left(\frac{\rho_q(\omega)}{\rho_r(\omega)}\right) \approx \frac{\rho_q(\omega)}{\rho_r(\omega)}. \end{cases} \tag{2}$$

The study of the complex resistivity of rocks and their spectral behaviour is thus a way to access additional information about the underground. Originally used in mineral exploration for ore body mapping, Pelton *et al.* (1978) suggested the use of the empirical Cole–Cole (CC) relaxation model (Cole & Cole 1941) to relate CC model parameters fitting the complex resistivity (CR) spectrum to medium properties based on earlier laboratory experiments (Madden & Cantwell 1967). He demonstrated that the CC model parameters describing the shape of the measured resistivity spectrum can help for the discrimination of the type of disseminated metallic particles and give an estimation of their concentration,by taking advantage of their characteristic CR frequency behaviour and their phase magnitude. Their resistivity magnitudes can be similar to other bodies but have different frequency behaviour, pointing out the major interest of the method. CC model became since one of the most popular empirical IP model. However, there are several kinds of empirical models describing the CR spectrum that are still in discussion according to their applications domain (see the work of Dias (2000) for a presentation of 12 existing models based on equivalent circuits). In a recent work, Liu *et al.* (2016) presented a detailed discussion about the performance of several relaxation models to fit a CR spectrum according to mineralization.

As well as for ore body discrimination, IP phenomena were shown to be linked to various kinds of physico-chemical properties of the media and more particularly linked to the pore space geometry and fluid interactions. IP method was used in various contexts as for hydrocarbon detection (Davydycheva *et al.* 2006; Veeken *et al.* 2009), hydrogeological studies (Börner *et al.* 1996; Ghorbani *et al.* 2009), contaminant detection (Vanhala 1997) and more recently in biogeophysical application as reviewed in the work of Kessouri *et al.* (2019).

To study the CR of the medium and its spectral behaviour, the use of a large frequency range is necessary. DCIP methods assume a static field (no time-variation) and EM/IP coupling issues can appear if DC hypothesis is not respected. EM induction increases with frequency, offset and depends on the wire-layout. Several empirical methods dealing with EM induction in DCIP surveys exist, as using EM removal techniques summarized in Routh & Oldenburg (2001). Nevertheless, in many DCIP field-scale studies, the frequency range is limited to be able to neglect EM induction using only unaffected data (Karaoulis *et al.* 2011; Orozco *et al.* 2012).

A rigorous solution to EM/IP coupling is to take into account the full-EM response of the ground by solving Maxwell equations and considering the cable layouts. Controlled Source Electromagnetic methods (CSEM) use the full-field EM responses of the underground excited by a galvanic or an inductive source to recover the resistivity of the ground. CSEM data can be processed equivalently in the time domain or frequency domain (Mörbe *et al.* 2020; Martin *et al.* 2020). As CSEM methods can be an ambiguous term, we will refer in this paper to all EM methods using an active EM source in the frequency range within approximately 1 mHz to 100 kHz and for investigation depths going from a few meters to a few kilometres. Contrary to the DCIP method, EM induction is not viewed as noise, but as an information fully taken into account to reconstruct the resistivity model. These kinds of methods are nevertheless numerically more demanding. They were intensively used for imaging hydrocarbon reservoirs in marine applications (Constable 2010). They were also used to image and monitor geothermal reservoirs (Darnet *et al.* 2020; Bretaudeau *et al.* 2021). The CSEM methods have a higher depth of investigation than the DC method. CSEM methods usually consider the electric resistivity to be a real and constant parameter by considering IP effects to be negligible.

However, in presence of IP phenomena, this assumption leads inversion to omit some crucial information on the medium properties. In their works (Mörbe *et al.* 2020) presents a large land-CSEM survey with data contaminated by sufficiently strong IP effects at low frequency from conductive graptolite shales to be noticed. Recently, some authors proposed CSEMIP inversion combining EM induction and IP for a constant CR in 2.5-D (MacLennan *et al.* 2014) and in 3-D (Commer *et al.* 2011). To our knowledge, only one research group worked to solve together EM induction and IP effects in 3-D considering a frequency-dependent resistivity based on an integral equation approach and the less common GEMTIP model (Zhdanov 2008; Zhengwei Xu & Zhdanov 2015; Zhdanov *et al.* 2018). Combining IP and CSEM methods are of increasing interest these late years to complete our knowledge of the medium in an increased range of frequencies. With recent improvements in instrumentation capabilities as well as the developments of high-performance computational facilities, the technical abilities to manage such complexity are spreading. Nevertheless, the need for CSEM tools able to handle such frequency-dependent CR without relying on a specific parametrization is still a necessity.

To recover IP parameters from CSEM inversion new challenges arise with the multiplication of parameters. At least, one additional parameter per cell is necessary to introduce IP for the simplest constant CR case. This case is similar to the simultaneous inversion of dielectric permittivity and conductivity for high-frequency data ($f > 100$ kHz) as imaginary resistivity can be expressed as a permittivity. Some authors as Lavoué *et al.* (2014) and Busch *et al.* (2012) developed some strategies to scale the parameters and precondition the inversion to reconstruct simultaneously electric conductivity and dielectric permittivity from Ground Penetrating Radar (GPR) data using full waveform inversion (FWI). For the general case of a frequency-dependent CR, a real and an imaginary resistivity per layer and per frequency is needed to fully describe IP phenomena. Keeping that kind of parametrization is unbearable as the inverse problem is already ill-posed in the majority of the cases and suffers from non-uniqueness of the solution. An appropriate model support is necessary to describe the medium with a reduced number of parameters as it increases proportionally with the number of frequencies. The choice of parametrization is of crucial importance to correctly scale the problem between each class of parameter (Nocedal & Wright 2006). Virieux & Operto (2009) highlighted in

their paper on FWI, the importance of the parametrization choice for multiparameter inversion considering targets and acquisition configurations. They presented how some parameters can be coupled or not, as some parameters can explain the same part of the data, whereas some are complementary.

We propose in the first part of this paper to present how IP is contaminating CSEM data set in the quasi-static frequency domain for a galvanic source. To better understand IP contamination in CSEM data sets, we present a 1-D sensitivity study of CSEM data to CR. At first, we discuss the simplest case of the electric field response of a homogeneous half-space with a constant CR and a CC based resistivity model to illustrate clearly the IP impact expected on a CSEM data set for a frequency-dependent CR case. The case of a chargeable conductive layer in a homogeneous background is then discussed to present large EM induction coupling arising with the increasing of the frequency, offset and conductivity.

In the second part of the paper, an inversion framework and a parametrization developed to retrieve the frequency-dependent CR based on the sensitivity analysis is presented. We demonstrate the feasibility of the method with 1-D synthetic examples using a 1-D inversion based on a semi-analytical (SA) code. The method is then extended to the 3-D case. The inversions of more complex 3-D synthetic models with 3-D frequency-dependent polarizable buried targets are presented, and the results are finally discussed.

2 SENSITIVITY STUDY

At first, we evaluate the sensitivity of CSEM data to CR in order to better understand the IP signature in the EM data and define an efficient way to derive them. We restrain our study here to the case of the electric field response of the underground induced by an inline horizontal electric dipole ($HED_{//}$) (galvanic transmitter) located at the surface. This is the classic case of ERT and SIP method in a Dipole–Dipole configuration, except that electromagnetic induction is fully taken into account. SIP method assumes to work in the static case, whereas CSEM methods use electromagnetic induction to investigate spatially the underground with several frequencies by varying the skin depth $\delta \approx 503\sqrt{\frac{\rho}{f}}$. The static case is respected when the offset r from the source is smaller than a wavelength ($\lambda_w = 2\pi\delta$) $r \ll \lambda_w$, corresponding to the 'near field', which is in opposition with the 'far field' where $r \gg \lambda_w$ corresponding to the plane wave domain used in the magnetotelluric method. Considering EM induction allows the scanning of the underground from the near to the far-field cases depending on the r/δ ratio.

Note that, if the magnetic field is considered to study IP, several limitations are expected to reconstruct the resistivity spectrum as the magnetic field in the near field is 'saturated' and has no sensitivity to the medium resistivity (Zonge & Hughes 1991). This limitation can also be observed for an inductive source on the electric field which vanishes in the near field. Furthermore, (García-Fiscal & Flores 2018) established in their study an improved capacity of (galvanic) SIP methods to solve Cole–Cole CR parameters compared to the in-loop transient electromagnetic method (TEM), which uses the magnetic field obtained at the centre of an induction loop, which thus mixes inductive and polarization current. Considering these first limitations, by focusing on the case of the electric field response from a galvanic source we expect an improved investigation of the CR spectrum especially at low frequencies.

We first study the sensitivity of IP in CSEM data for a constant CR half-space with a resistivity phase ϕ_{cpx} of -100 mrad. This value of phase is in the range of what can be expected in measurements over disseminated metallic particles ore bodies as presented by Pelton *et al.* (1978) or Liu *et al.* (2016). We compare in the following examples a purely real and constant resistivity model to a CR model with a tenth ratio between imaginary and real resistivity part, as described by eq. (2), with $\phi_{\text{cpx}} \approx \frac{\rho_q}{\rho_r}$. Note that we use ϕ_{cpx} notation to describe the CR phase, which should not be mistaken in the following argumentation with the observed data field phase delay denoted φ.

In order to quantify IP impact in CSEM data, we introduce here the term IP effect Δ_{ip} as used in Qi *et al.* (2019). Lets consider $F^n()$ an operator that extracts the real part, the imaginary part, the amplitude or the phase of the electric field for a given spatial component n. The IP effect measures the relative variation between a response $F^n(E_{\rho^*})$ of a model taking into account a CR (that can be frequency-dependent) to the electric field response $F^n(E_{\rho_0})$ of a real and constant resistivity as used for a DC or CSEM survey. The response difference due to the IP effect is normalized by the amplitude of the total electric field response for the corresponding real and constant resistivity model at zero frequency. Normalization by the total amplitude allows to avoid giving importance to weak anomalies that are irrelevant in comparison to the total measured field (i.e. case of the electric field in quadrature phase towards the DC limit, where its quadrature phase response vanishes for a real resistivity but not its total field). In the case of the IP effect shown for the electric field phase, the absolute difference is kept instead of a relative IP effect. IP effect is defined for each observable as :

$$\Delta_{ip}(\omega) = \left| \frac{F^n(E(\omega))_{\rho^*(\omega)} - F^n(E(\omega))_{\rho_0}}{\left|E(\omega)_{\rho_0}\right|} \right| \times 100$$
$$\text{if } F^n() \text{ extracts amplitude, real or imaginary part in the direction n,} \quad (3)$$

or,

$$\Delta_{ip}(\omega) = \left| F^n(E(\omega))_{\rho^*(\omega)} - F^n(E(\omega))_{\rho_0} \right|$$
$$\text{if } F^n() \text{ extracts the phase in the direction n.} \quad (4)$$

Frequency-dependent CR is studied by considering the response of a medium with a Cole–Cole relaxation CR model $\rho^*(\omega)$ and is compared to the medium 'without IP', defined as the medium with a constant and real resistivity ρ_0 in the static case and corresponding to the first CC parameter.

2.1 Constant resistivity homogeneous half-space

1-D responses are computed using a 1-D semi-analytical (SA) code based on *em1d* code (Kim *et al.* 1997). Fig. 1 presents electric field responses using normalized amplitude and phase spectra (left), or normalized in-phase and quadrature-phase representation (right), as a function of r/δ, with r the source-receiver offset and δ the skin depth. Responses are normalized by their total amplitude in the static case (i.e. using the value for the smallest ratio computed $r/\delta < 10^{-1}$). This kind of representation allows visualizing the response from the near field (DC hypothesis) ($r/\delta \ll 1$) to the far-field ($r/\delta \gg 1$), independently to the resistivity amplitude of the half-space or the dipole moment. Electric field on a homogeneous half-space with respect to r/δ shows an equivalent effect of the offset or the frequency variation, as skin depth is proportional to the inverse of the frequency square root.

The in-phase electric field is generally attributed to galvanic effects in the medium, whereas quadrature response is attributed to EM induction. The amplitude and phase of the electric field are a

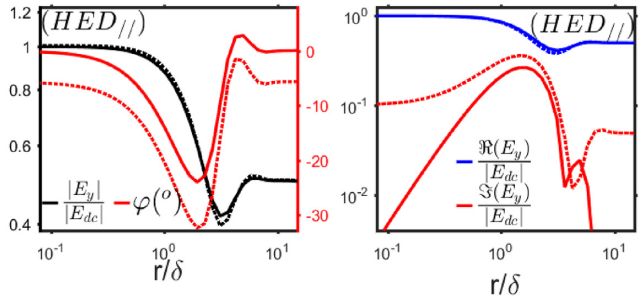

Figure 1. Normalized amplitude and phase (left-hand panel) and normalized in-phase and quadrature (right-hand panel) electric field responses for an inline HED, considering a 100 Ω.m real resistivity model with and without −100 mrad of CR phase delay. Dotted lines represent the CR model response whereas solid lines represent the real and constant resistivity response (without IP effect).

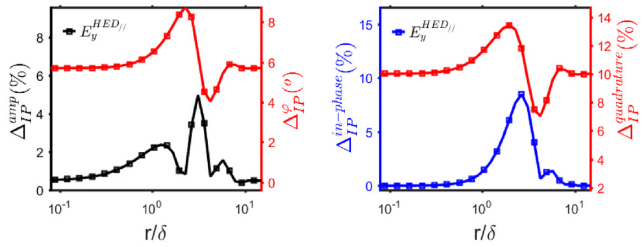

Figure 2. IP effect on amplitude and phase delay (left-hand panel) and on in-phase and out-of-phase (right-hand panel) electric fields on a 100 Ω.m real resistivity homogeneous half-space with −100 mrad of CR phase delay.

mix of both parts. We choose to present in a first example both representations for the electric field response of a half-space to have a better understanding of IP effect on each CSEM observable. We can see on Fig. 1 that IP effect caused by a constant CR with $\phi_{\text{cpx}} = -100$ mrad has a very low effect on the amplitude as responses are almost superimposed, except in the transition zone ($1 \leq r/\delta \leq 5$). IP effects presented in Fig. 2 are limited around 1–2 per cent of electric amplitude except in the limited bandwidth of the transition area where it can reach 5 per cent. The real part of the electric field reflects mainly its amplitude due to low quadrature phase response, but IP effects are slightly higher on the real part. Contrary to electric field amplitude, IP effects on the electric field phase can easily be differentiated. Indeed, we observe that IP effects create a strong phase delay compared to the real and constant resistivity case. Phase effects around 5.7° (5.7 ° = 100 mrad) are observed on the complete spectrum, with a maximum around 8.5° in the transition zone for $HED_{//}$. A minimum is observed around $3\frac{r}{\delta} \approx \frac{\text{wavelength}}{2}$ due to a sign reversal of the quadrature electric field. Note that the electric field phases are shown in degree rather than using milliradian, as EM data are prone to large phase variations compared to SIP data. Furthermore, it allows to better differentiate the data (electric field phase) to the medium parameter (CR phase) and avoid confusion as they cannot be directly related in CSEM data (impacted by EM induction) contrary to SIP data.

Considering grounded electric dipole sources, the phase at low frequency is entirely caused by IP phenomena without amplitude variation in the near field domain as there is no EM induction in the static limit. An apparent CR norm and an apparent phase can thus be deduced from the electric field using a geometric coefficient. This is the principle of the DCIP method, where EM induction is neglected. Nevertheless, when r/δ becomes superior to 0.1, phase delay caused

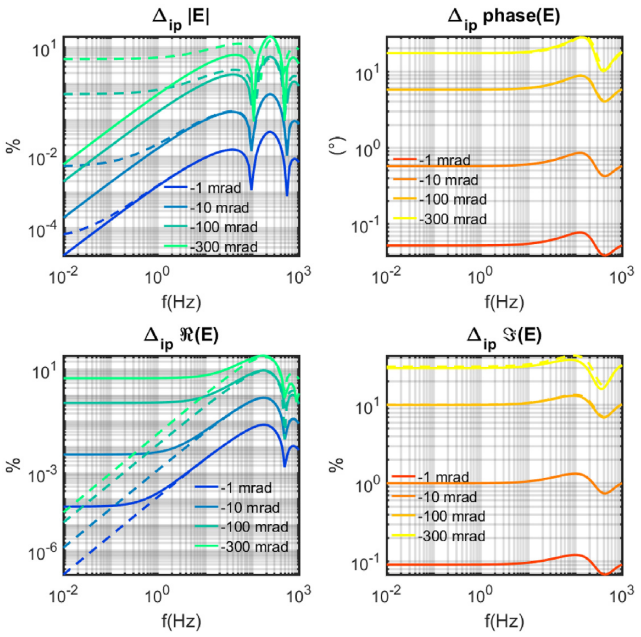

Figure 3. IP effect observed on the electric field amplitude and phase (top left and right) and on the in-phase and out-of-phase electric field response (bottom left and right) when increasing CR phase introduced in the medium by keeping the CR norm $|\rho^*|$ constant (solid lines) or keeping the real part ρ_r constant (dashed lines) at a value of 100 Ω.m. An offset of 1500 m is used here.

by EM induction in the half-space gradually adds up to the electric field as quadrature currents increase up to $r/\delta \approx 1$ where EM induction is expected to reach a maximum (Spies & Frischknecht 1991). In these cases, the DC hypothesis does not hold anymore. It becomes thus crucial to take EM induction into account by modelling the full EM response to be able to separate IP information from EM coupling. As an illustration, for a homogeneous half-space, a phase delay due to EM induction up to 25° can be observed around $r/\delta \approx 1$ which is larger than the anomalies due to IP effects (Fig. 1a).

IP effects observed on the electric field phase are due to a strong impact on quadrature electric field compared to in-phase response as seen in Fig. 1. Indeed, relaxation currents due to medium chargeability introduced by the CR are delayed compared to the injected current. We can see in Fig. 2 that the IP effect on the quadrature response represents around 10 per cent of the total electric field on the complete spectrum, whereas as observed on the amplitude, the in-phase IP effect reaches a significant value up to 10 per cent only on a narrow frequency window in the transition zone. This peak is explained by an additional coupling between IP effect and EM induction in the medium.

2.1.1 *Resistivity phase effect*

In the previous section we introduced ρ_q through a constant phase of –100 mrad by keeping constant ρ_r. Fig. 3, compares IP effect for various CR phase for a half-space and the $HED_{//}$ case at constant $|\rho^*|$ or at constant ρ_r. For each observable, proportionality can be observed with the phase increase. Proportionality between the CR phase and electric field response is observed, involving that a –10 mrad half-space produces around 10 times less IP effect than a –100 mrad half-space. As CR phase delay decreases, the IP effect is thus weakening, becoming lower than 1 per cent of relative anomaly for a –10 mrad of CR phase.

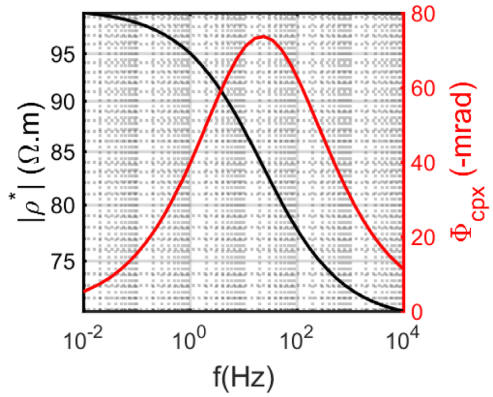

Figure 4. CR spectra for a Cole–Cole relaxation model $\rho_0 = 100\,\Omega$.m, $\rho_\infty = 70\,\Omega$.m, $m = 0.3$, $\tau = 0.01\,s$, $c = 0.5$.

A fundamental difference can be observed between the amplitude and the real part observable compared to $|\rho^*|$ constant or ρ_r constant cases (see Fig. 3). Indeed, towards DC limit the curves become largely distinct. In the case of $|\rho^*|$ constant, increasing the phase has a weak impact at low frequencies on the electric amplitude, whereas keeping ρ_r constant when increasing the phase has a larger impact at low frequency with an IP effect tending to an asymptote. This observation can also be made for the real/imaginary part observables, unless it is the $|\rho^*|$ constant case that is impacted at low frequency by varying the phase. At high frequency, IP/EM coupling intervenes and explains large variations in both cases.

Looking closer to the radial static response E_{radial} of an inline HED source on a homogeneous half-space at DC limit, we have:

$$E_{\text{radial}} = \frac{2I\rho*}{2\pi r^3}. \tag{5}$$

It is straightforward that the real part of the electric field in the static limit is directly proportional to ρ_r and the imaginary part to ρ_q, whereas if looking for the amplitude and the electric field phase response we obtain:

$$|E_{\text{radial}}| = \frac{2I}{2\pi r^3}\sqrt{\left(\rho_r^2 + \rho_q^2\right)} = \frac{2I|\rho^*|}{2\pi r^3} \tag{6}$$

$$\varphi_{E_{\text{radial}}} = \text{atan}\left(-\frac{\rho_q}{\rho_r}\right) \approx \phi_{\text{cpx}}. \tag{7}$$

It highlights that when looking at the amplitudes and phases of the electric field responses, evaluating the IP effect by comparing the model at $|\rho^*|$ constant should be preferred instead of keeping ρ_r constant and the opposite when looking at real/imaginary parts of the electric field. Reformulated in a more practical way, it highlights that varying the CR phase by keeping the norm constant perturbs less the electric amplitude and reciprocally for the real/imaginary part.

In this section, we have shown that a considerable IP effect caused only by the imaginary part of CR can be observed in CSEM data. IP effects magnitude is controlled by the CR phase ϕ_{cpx}. The presence of an imaginary resistivity ρ_q impacts mainly the phase of the data and has a weak effect on the amplitude of the electric field response, which shows significant IP effects only within a limited bandwidth in the transition zone due to supplementary coupling between EM and IP effects.

2.2 Frequency dependent complex resistivity half-space

In presence of IP phenomena, a frequency dependence of the CR can be observed, even though it is often considered constant in

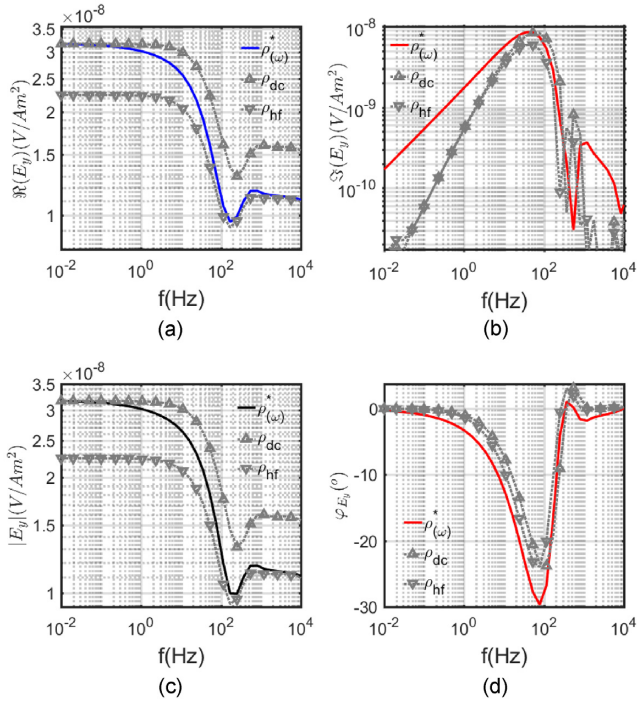

Figure 5. Electric field in-phase (a) and quadrature (b) for a C-C polarizable half-space for an in-line HED source at 1000 m offset; CR model response is compared to real and constant resistivity model responses at DC (ρ_0) and HF (ρ_∞) C-C model boundaries. Panels (c) and (d) show the same response as (a) and (b) but as electric field amplitude and phase.

a first approximation. We show in Fig. 5 the electric field of a homogeneous half-space for a galvanic source $HED_{//}$ assuming a frequency-dependent CR based on a Cole–Cole relaxation model (Fig. 4, eq. 8):

$$\rho^*(\omega) = \rho_0\left[1 - m\left(1 - \frac{1}{1 + (i\omega\tau)^c}\right)\right]. \tag{8}$$

The four CC parameters used in the following example to describe the half-space are the resistivity at DC current $\rho_0 = 100\,\Omega$.m corresponding to the low-frequency asymptotic limit, the intrinsic chargeability $m = 0.3$, a short relaxation time constant $\tau = 0.01$ +, s, related to the peak phase frequency, and the frequency dependence exponent $c = 0.5$. As intrinsic chargeability is defined as $m = \frac{\rho_0 - \rho_\infty}{\rho_\infty}$, we obtain the high-frequency asymptotic value, expected for this CC relaxation model, at $\rho_\infty = 70\,\Omega$.m. The peak phase is expected at the frequency $f_{\text{peak}} = \frac{1}{2\pi\tau(1-m)^{\frac{1}{2c}}} = 23$Hz (Fiandaca *et al.* 2018).

Using frequency domain analysis we can directly see in Fig. 5(a) the gradual behaviour of the in-phase electric field between the two asymptotic values defined by the CC resistivity model. In-phase electric field gradually fits the homogeneous half-space response from ρ_0 to ρ_∞, following essentially the real resistivity variation. Indeed, we saw previously for the homogeneous case that the real part of the electric field is weakly sensitive to ρ_q. Considering the CC resistivity model shown in Fig. 4 and taking the DC resistivity half-space as a reference, the IP effect on the in-phase electric field increases from around 1 per cent at low frequency (Fig. 6), where ρ_r tends to the reference model ρ_0, to reach approximately 30 per cent at high frequencies with a maximum in the transition zone. As EM induction in a simple half-space is weak, the electric field amplitude reflects essentially the real part of the electric field

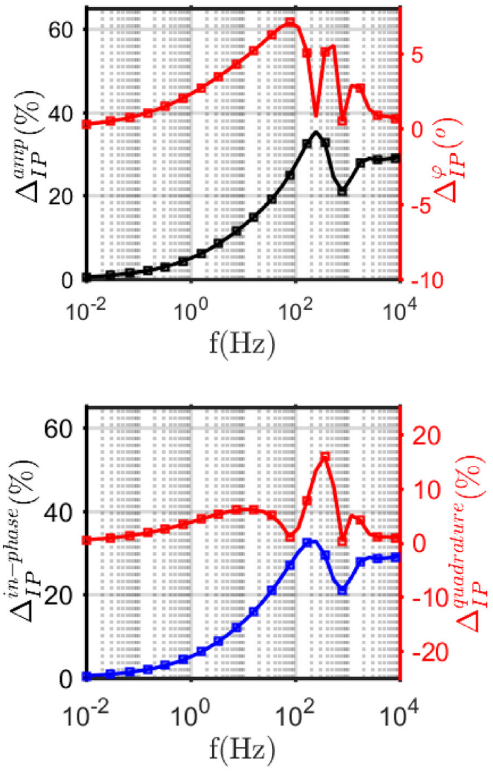

Figure 6. IP effect on amplitude and phase (top panel) or in-phase and quadrature (bottom panel) EM responses for the CC resistivity half-space model.

as the imaginary part is weak (Fig. 5b). The gradual behaviour observed for the amplitude and in-phase part of the electric field between the responses of ρ_0 and ρ_∞ model is less obvious looking at the quadrature phase response. Indeed, the variation of ρ_r with the frequency affects the EM induction, which is mixing up with the additional phase delay due to the frequency-dependent CR phase ϕ_{cpx} variation. We can see the IP effect on the electric phase in Fig. 5(d) showing an additional phase delay proportional to the Cole–Cole phase model, coupled with the effect of the variation of the CR norm which induces a slight frequency shift of the phase curves.

Fig. 5 shows that if we consider a real and constant resistivity in CSEM study with a broad frequency range and in presence of IP, it can lead to a significant modelling error. Here, strong IP effects due to ρ_r variations are observed compared to a constant and real resistivity model. Note that these observations can only be made by observing several frequencies and depends on the reference model. IP effects due to ρ_r variations are stronger on the in-phase component if compared to IP effects due to ρ_q and can represent up to 30 per cent of the total amplitude instead of a localized maximum around 16 per cent for the quadrature electric field. CSEMIP data will be more sensitive to the CR norm, or its real part variations compared to the imaginary part or the phase variations because they induce weaker IP effects on the electric quadrature field or electric field phase. Considering the frequency dependence or the CR and behaviour seen in Fig. 5, we see that a large spectrum is necessary to characterize the complex resistivity variations. If investigation frequency does not include the frequency range where ρ^* is impacted by frequency variations, main IP information can be missed. These observations highlight the necessity to choose carefully the frequencies used, relative to the target and keeping in mind the fact that in a real field-scale survey only a partial information of the CR spectrum would be accessible.

2.3 Buried layer

Sensitivity to IP effects will depend on several factors in the case of a buried target. They are linked to the fundamental difference between geometrical and frequency sounding. DC method uses geometrical sounding to control investigation depth by varying TX-RX offset, whereas CSEM methods use frequency sounding and more often a complementary mix of both to control investigation depth. Indeed, the depth of investigation depends on the skin depth in the medium, decreasing with increasing conductivity and frequency. Sensitivity to the buried body depends on the offset and the frequency used. EM data will lose their sensitivity to the target at too short offset, depending on the survey geometry, or at skin depth shorter than the target depth. Fig. 7 shows the electric field of a 100 m thick conductive layer, considering a real or a complex constant resistivity, embedded at 100 m depth in a homogeneous half-space at 100 Ω.m. Real part of the resistivity in the conductive layer was chosen with a 1: 10 ratio with the background with $\rho_r = 10\,\Omega.\text{m}$, and an imaginary part ρ_q corresponding to $\phi_{\text{cpx}} = -100\,\text{mrad}$. As the sensitivity of the target is varying with the offset, we choose to present a medium offset of 570 m corresponding approximately to five times the depth of the target and being approximately an offset of a skin depth separation ($\delta \approx 503\sqrt{\rho/f}$) at 100 Hz (in the background). This choice ensures a sufficient offset for geometrical investigation and for studying EM induction coupling. A nearer offset would result in a near field case on the complete frequency range or an insufficient geometrical investigation depth, whereas farther choices would result in ranges out of the scope of this article as it would generate weaker amplitude responses or would concern plane-wave methods as for magnetotelluric methods (Chave & Jones 2012). We compare on Fig. 7 in-phase and quadrature parts of the electric field for the real resistivity case E^r and for a constant CR case E^*. Furthermore, electric field of the real resistivity background E^{bg} is plotted with the IP response component. IP response is separated here analogously to the primary/secondary field separation $E_s^r = E^r - E^{bg}$, commonly used in CSEM (Newman & Alumbaugh 1995) and noted $R_{\Delta\text{ms}} = E^* - E^r$. Similar observations similar to the half-space case can be made. We see negligible effects of the presence of ρ_q component on the in-phase electric field with a 7 per cent maximum on a limited frequency range around 200 Hz, whereas an effect around 8 per cent can be observed on the quadrature electric field under 200 Hz (Fig. 7c). For frequencies higher than 2.5 kHz, we can see the response of the layer slowly tending to the response of the homogeneous background case as the skin depth in the homogeneous background is decreasing below the depth of the target. A major difference with the half-space case is the strong EM induction response of the layer, corresponding to the out-of-phase secondary field $\Im(E_s^r)$ from the real resistivity case, much larger than in the homogeneous case. It results in a competition between the IP effects and EM induction at high frequencies. For this particular case, EM induction becomes greater than $E_{\Delta ip}$ on the quadrature component of the electric field around 10 Hz, leading to an IP effect becoming slowly negligible.

This case illustrates that in intervals where EM induction is too large compared to IP effects, the information due to ρ_q would not, or hardly, be recoverable. It implies that the domain where IP effects due to ρ_q and EM induction are distinguishable will depends on the amplitude of both effects and on the offset from the source

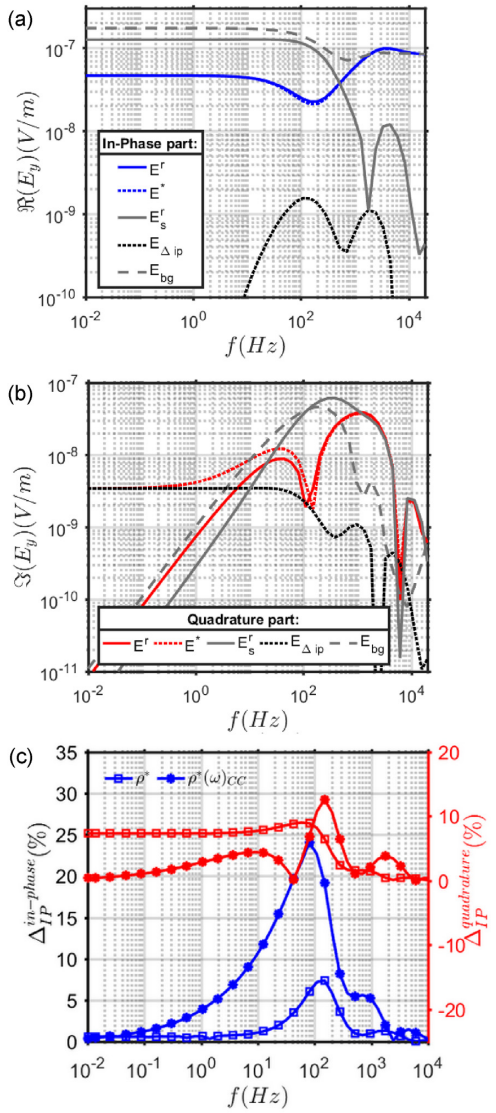

Figure 7. In-phase (a) and out-of-phase (b) electric fields of a constant 10 Ω.m layer with (E^r) and without (E^*) a –100 mrad CR phase, in a 100 Ω.m background at an offset of 570 m. Responses were decomposed into the primary field (E_{bg}), the real resistivity model secondary field (E^r_s) and the IP contribution $E_{\Delta ip} = E^* - E^r$. (c) IP effect observed for the In-phase (blue) and out-of-phase (red) electric fields of the constant CR layer model and a frequency dependent CR layer model based on the previous CC model ($\rho_0 = 100\,\Omega.\text{m}$, $\rho_\infty = 70\,\Omega.\text{m}$, $m = 0.3$, $\tau = 0.01\,s$, $c = 0.5$).

where EM induction arises. The study of the CR behaviour at high frequencies will be helped by offsets as short as possible according to geometrical investigation and depth of the target, to avoid as possible the domain where EM induction is dominant.

Through these examples, we saw that even if the full EM responses are accounted for in IP studies and before considering signal-to-noise ratio, there are strong limitations on which additional information would be recoverable from a CSEM IP survey:

(i) Medium without ρ_r frequency dependence would be harder to recover, as IP information is supported only by the quadrature response with a lower amplitude.

(ii) IP effect over the quadrature electric field due to ρ_q becomes negligible compared to EM induction arising from medium anomalies at high frequencies and large offsets.

(iii) Sensitivity to anomalous body is a function of the offset and frequency compared to its depth and size, which will limit the frequency range where the CR spectrum of the target is recoverable.

Accessing to IP information is a challenge in several ways. Even in a perfect case, it will often lead to recover only incomplete information, limited by EM induction in the medium, depth of the target, survey design and shape of the resistivity relaxation. However, we saw that a significant IP effect can still be observed in the data. These data could be strongly coupled to EM induction, especially in the case of deep targets requiring long offsets. In order to retrieve a CR spectrum in these cases, it is necessary to properly consider the inversion of IP and EM simultaneously.

3 INVERSION OF COMPLEX RESISTIVITY

In this part, we describe the inversion framework proposed to infer a 3-D CR model from EM data. Our work relies on the implementation of CR modelling and inversion into the code POLYEM3D (Bretaudeau *et al.* 2021). This code is a 3-D finite-difference parallel code for modelling and inversion of CSEM and MT data in the frequency domain. We first introduce briefly the essentials of the original code and the straightforward implementation of CR to the forward problem. For the sake of clarity, and to assess and validate our inversion framework with reasonable computational times, we investigated the multiparameter inversion behaviour through a 1-D layered model inversion. We described through 1-D synthetic examples how we established an appropriate multiparameter parametrization and inversion strategy of the frequency-dependent CR. Finally, the approach is extended to 3-D, and we present the application to a more complex 3-D synthetic example.

3.1 Method

The code POLYEM3D solves electrical formulation of Maxwell equation with a scattered field approach (eq. 9, Newman & Alumbaugh 1995). The primary field $\boldsymbol{E_p}$ defined as the electric field in a 1-D reference medium σ_p, is solved using the accurate and fast semi-analytical code mentioned in Section 2.1 (*em1d*, Kim *et al.* 1997) whereas the scattered or secondary field $\boldsymbol{E_s}$ is solved on an irregular Cartesian grid by a FD scheme (eq. 9) on a staggered grid formulation (Streich 2009).

$$\nabla \times \nabla \times \boldsymbol{E_s} + i\omega\mu_0\sigma\,\boldsymbol{E_s} = -i\omega\mu_0(\sigma - \sigma_p)\boldsymbol{E_p}. \tag{9}$$

The imaginary number is noted i, ω represents the angular frequency and μ_0 the magnetic permeability in the vacuum. Separation of the primary and secondary fields allows to avoid singularity of the sources and manage numerical errors due to the fast decrease of the primary field from the source. Electric field vectors of size $3N$ contain all three components of the fields on the staggered grid with N the number of cells.

The medium is originally described by a complex conductivity vector σ with the dimension of the forward grid N, contributing to a diffusion and a propagation term through a constant and real conductivity σ^r and relative permittivity ϵ_r, with ϵ_0 the dielectrical permittivity of the vacuum:

$$\sigma = \sigma^r + i\omega\epsilon_r\epsilon_0. \tag{10}$$

The forward problem is reduced to a linear system of equations of the form $\boldsymbol{A}x = b$, with x the vector of secondary field on the staggered grid, b corresponding to a secondary source term $(\sigma - \sigma_p)\boldsymbol{E_p}$,

and $\boldsymbol{A}$ the sparse system of FD equations ruling the problem on the staggered grid with thirteen non-zero terms per line. The system is then solved using a parallel direct solver (MUMPS (Amestoy *et al.* 2001, 2019) or WSMP (Gupta 2000)). A rigorous interpolation (Shantsev & Maaø 2015) taking into account the sharp discontinuities at the air/ground interface, is used to obtain the field response at the receiver.

Frequency domain CSEM is very well suited to implement IP effects as we are modelling independently each frequency, contrary to the time domain method. We straightforwardly adapted the forward problem to a frequency-dependent CR input model. Real and imaginary parts of the resistivity are used to describe the medium for each frequency. A reformulation of the propagation term to integrate the imaginary part of the CR as an effective permittivity ϵ_{eff} is done. σ^r in eq. (10) is replaced by a complex conductivity σ^* and real and imaginary parts are separated:

$$\sigma(\omega) = \overbrace{\sigma^r(\omega) + i\sigma^q(\omega)}^{\sigma^*} + i\omega\epsilon_r\epsilon_0 \tag{11}$$

$$= \sigma^r(\omega) + i\omega\epsilon_{\text{eff}}(\omega) \qquad \text{with } \epsilon_{\text{eff}} = \epsilon_r + \frac{\sigma^q(\omega)}{\omega\epsilon_0}. \tag{12}$$

Solving the inverse problem consists here to seek for a model minimizing an objective function χ (eq. 13), with a data associated function χ_d and one or several model regularization terms χ_m.

$$\chi = \chi_d + \lambda\chi_m. \tag{13}$$

The data minimization term usually consists of the norm of the data vector residuals between the calculated and the observed data d^{cal} and d^{obs}, respectively, weighted by a diagonal matrix W_d composed by the inverse of the data standard deviation. Data vectors are of the size N_d depending on the number of frequencies, transmitters (TX), receivers (RX) and components considered. We restrain our present work to the use of a L2 norm (eq. 14):

$$\chi_d = \frac{1}{2}||W_d\left(d^{\text{cal}} - d^{\text{obs}}\right)||^2. \tag{14}$$

The inverse problem is solved iteratively with a deterministic linearized descent method. As the inverse problem can be overdetermined, or more frequently underdetermined for large problems, a regularization is required to stabilize the problem and converge to a solution. Many types of regularization are possible, depending on the specificities of the problem and prior information available. Several types of common regularization are available in POLYEM3D. We use a Tikhonov stabilizing functional with a maximum smoothness condition (eq. 15) taking the L_2 norm of the Laplacian of the model deviation from a reference model (Grayver *et al.* 2013) with λ a Lagrange multiplier acting as a trade-off parameter between data and model regularization. The reference model is chosen here as the model at the previous iteration. A minimum norm stabilizing functional (eq. 16) is also combined with the smoothing constraint in the following 1-D cases to better regularize the iteration step in multiparameter cases as the maximum smoothness condition does not constrain the length of the step of the model perturbation during the iterative process as soon as the perturbation is smooth.

$$\chi_m^{smooth} = ||\nabla^2(m - m^{ref})||_2^2 \tag{15}$$

$$\chi_m^{norm} = ||m - m^{ref}||_2^2, \tag{16}$$

with m the vector of model parameters describing the medium of dimension N_m and depending on the inversion domain size and parametrization. Usually, a smaller grid with variable transformation is used as inversion grid comparatively to the forward grid.

The optimization algorithm is a preconditioned gradient-based descent method implemented through a reverse communication algorithm, combined with a line search based on a bracketing strategy (Nocedal & Wright 2006; Métivier & Brossier 2016). It requires at each iteration the computation of the cost function χ and its gradient $\partial_m\chi$. Local optimization using gradient-based methods solves iteratively a problem at the iteration k and starting from a model m_0 with a defined step Δm in the descent direction determined by the reversed gradient of the cost function:

$$m_{k+1} = m_k + \Delta m_k \tag{17}$$

$$m_{k+1} = m_k - \alpha\partial_m\chi. \tag{18}$$

We denoted partial derivatives with respect to a variable using a compact notation. The partial derivative by m is thus noted $\partial_m = \frac{\partial}{\partial m}$. The optimal descent step length α is determined using a line-search technique respecting the Wolf-conditions (Nocedal & Wright 2006) ensuring the objective function to decrease of a sufficient amount using the curvature condition. The gradient of the data cost function for an L2 norm needs estimation of the sensitivity matrix J and the data residual vector Δd expressed as:

$$J_{i,j} = W_{d_i}\frac{\partial d_i}{\partial m_j} \quad \text{with } \mathrm{i} = 1, ..., N_d \quad \text{and } \mathrm{j} = 1, ..., N_m$$
$$\partial_m\chi_d = \Re(J^\dagger W_d\Delta d) \quad \text{with}$$
$$\Delta d = d^{\text{cal}} - d^{\text{obs}}. \tag{19}$$

† denotes the transposed conjugate operator. Derivatives expressions of the regularization cost function can be found in Grayver *et al.* (2013).

Gauss–Newton (GN) optimization which has a greater convergence rate, takes advantage of the approximated Hessian to solve the model step and neglect the second-order terms compared to full Newton method. The data part of the approximated Hessian is expressed as $\boldsymbol{H} = \frac{\partial^2\chi_d}{\partial m^2} = \Re(J^\dagger J)$. The Hessian helps to counterbalance the sensitivity gap between parameters. Considering a linear problem and taking the derivative of the second-order Taylor expansion of the data misfit function only, we have a solution for Δm respecting:

$$\boldsymbol{H}\Delta m = -\partial_m\chi_d. \tag{20}$$

For small problem as following 1-D examples, the approximated Hessian can directly be inverted to find the optimal step size. In order to take into account for non linearity of the problem, a line-search is undertaken to obtain an optimal step α ($\alpha > 0$) and the model at next iteration. The final equation including regularization terms solved to determine next iteration is:

$$m_{k+1} = m_k - \alpha\left[\Re(J^\dagger J) + \lambda\frac{\partial^2\chi_m}{\partial m^2}\right]^{-1}(\partial_m\chi_d + \lambda\partial_m\chi_m). \tag{21}$$

3.2 1-D complex resistivity inversion

In this section, we focus on the 1-D problem allowing reasonable memory usage and fast computation. The multiparameter problem of CR could easily be studied compared to larger 3-D problems. Jacobian computation was done explicitly using perturbation method with central point difference. Perturbation was chosen as 1 per cent of the resistivity to ensure a slight variation in the data and account for linearity approximation.

3.2.1 Parametrization

Considering at first a constant CR, the model parameter vector m contains $2N_{\text{inv}}$ real parameters with N_{inv} the number of inverted cells in the medium. m contains the CR of the medium separated into amplitude and phase of the CR. Different parametrizations can be used and the logarithm of these parameters will be investigated here as it constrains the positiveness of the solution. To respect the parametrization choice, some change of variables should be carefully applied to the Jacobian depending on the original formulation. As we are using for the 1-D case the perturbation method to obtain the Jacobian, we can straightforwardly perturb the respective parameters to solve it and obtain the gradient from eq. (19). Otherwise, change of variables for the gradient can be achieved using the chain rule (as it is necessary for the 3-D problem):

$$\partial_\rho \chi = \frac{\partial \chi}{\partial \rho} \tag{22}$$

$$\partial_m \chi = \frac{\partial \rho}{\partial m}\frac{\partial \chi}{\partial \rho} \tag{23}$$

In our case we want at first a formulation to invert the parameters $|\rho^*|$ and ϕ_{cpx} with m:

$$m_{|\rho^*|,\phi_{\text{cpx}}} = \begin{pmatrix} |\rho^*| \\ \phi_{\text{cpx}} \end{pmatrix} \tag{24}$$

The gradient (or the Jacobian) is calculated with respect to ρ_r and ρ_q separately and a change of variable is applied to obtain the desired parametrization.

The cost function depends on both variables in the CR case:

$$d\chi = \frac{\partial \chi}{\partial \rho_r} d\rho_r + \frac{\partial \chi}{\partial \rho_q} d\rho_q \tag{25}$$

Both parts of the gradient of the cost function with respect to the norm and the phase of the CR can be expressed for each cell as:

$$\begin{aligned} \frac{\partial \chi}{\partial m_{|\rho^*|}} &= \frac{\partial \rho_r}{\partial |\rho^*|}\frac{\partial \chi}{\partial \rho_r} + \frac{\partial \rho_q}{\partial |\rho^*|}\frac{\partial \chi}{\partial \rho_q} \\ \frac{\partial \chi}{\partial m_{\phi_{\text{cpx}}}} &= \frac{\partial \rho_r}{\partial \phi_{\text{cpx}}}\frac{\partial \chi}{\partial \rho_r} + \frac{\partial \rho_q}{\partial \phi_{\text{cpx}}}\frac{\partial \chi}{\partial \rho_q} \end{aligned} \tag{26}$$

Using the real and imaginary part in its cosine/sine formulation, we can differentiate each term with respect to amplitude/phase of CR into the following matrix:

$$\begin{aligned} \begin{pmatrix} \frac{\partial \rho_r}{\partial |\rho^*|} & \frac{\partial \rho_q}{\partial |\rho^*|} \\ \frac{\partial \rho_r}{\partial \phi_{\text{cpx}}} & \frac{\partial \rho_q}{\partial \phi_{\text{cpx}}} \end{pmatrix} &= \begin{pmatrix} \frac{\partial |\rho^*|\cos(\phi_{\text{cpx}})}{\partial |\rho^*|} & \frac{\partial |\rho^*|\sin(\phi_{\text{cpx}})}{\partial |\rho^*|} \\ \frac{\partial |\rho^*|\cos(\phi_{\text{cpx}})}{\partial \phi_{\text{cpx}}} & \frac{\partial |\rho^*|\sin(\phi_{\text{cpx}})}{\partial \phi_{\text{cpx}}} \end{pmatrix} \\ &= \begin{pmatrix} \cos(\phi_{\text{cpx}}) & \sin(\phi_{\text{cpx}}) \\ -|\rho^*|\sin(\phi_{\text{cpx}}) & |\rho^*|\cos(\phi_{\text{cpx}}) \end{pmatrix} \end{aligned} \tag{27}$$

Gradient with respect to amplitude and phase of the resistivity is finally expressed from the real/imaginary form of the gradient using for each term $j = 1,..., N_{\text{inv}}$:

$$\frac{\partial \chi_j}{\partial m_{|\rho_j^*|,\phi_{\text{cpx}_j}}} = \begin{pmatrix} \cos(\phi_{\text{cpx}_j}) & \sin(\phi_{\text{cpx}_j}) \\ -|\rho_j^*|\sin(\phi_{\text{cpx}_j}) & |\rho_j^*|\cos(\phi_{\text{cpx}_j}) \end{pmatrix} \begin{pmatrix} \frac{\partial \chi_j}{\partial \rho_{r_j}} \\ \frac{\partial \chi_j}{\partial \rho_{q_j}} \end{pmatrix} \tag{28}$$

3.2.2 Multistage workflow

With CR arises significantly the need to manage high number of parameters and non-uniqueness of the solution, especially in a frequency-dependent case as we add more unknowns to an already undetermined problem. Stabilizing the inversion to lead optimization to the rightful model is of crucial importance. The method used to constrain optimization is to take advantage of the differences in IP effects related to the variations of the amplitude and phase of CR in CSEM data. From the sensitivity study, we know that the impact of ϕ_{cpx} on the amplitude of the electric field is weak considering a similar $|\rho^*|$. To take advantage of this particularity, a multistage approach is developed allowing the management of real and imaginary CR parts independently:

(i) A first stage (1), consists in inverting the amplitude of the electric field to obtain the amplitude of the CR $|\rho^*|(\Omega.\text{m})$.

(ii) A second stage (2), inverts the residual remaining on the electric field phase to solve the CR phase $\phi_{\text{cpx}}(\Omega.\text{m})$ of the model.

The amplitude/phase parametrization of the electric field was preferred over the separation of real/imaginary parts as amplitude comprises a mix of both galvanic and induction information contained in the data, contrary to the real part of the electric field which is mainly associated to galvanic effects in the medium.

Table 1. Properties of the three layers CR model, with h the thickness of the layer.

Layer #	h (m)	$\lvert\rho^*\rvert(\Omega.\text{m})$	$-\phi_{\text{cpx}}$ (mrad)
1	100	100	0
2	100	10	100
3	∞	40	0

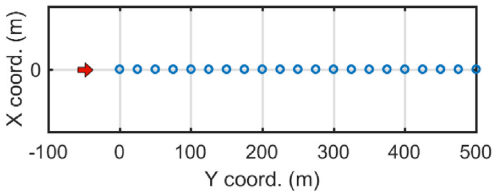

Figure 8. CSEM synthetic survey geometry using a 500 m profile of 21 receivers (blue circles) and a HED source oriented in-line, in the Y-direction (red arrow).

3.2.3 Constant complex resistivity model inversion

A 3-layers model is inverted with a conductive middle layer of 10 Ω.m and a resistivity phase of –100 mrad (Table 1). Observed data were generated with the same 1-D SA code and are inverted using a GN algorithm. During our developments, the GN method had proven better convergence rates and a better handling of the multiparameter problem due to the natural scaling properties of the inverse Hessian application compared to the steepest descent method using only the gradient, or other 2nd order optimization methods as L-BFGS (Métivier & Brossier 2016).

Synthetic survey geometry is a 500 m profile of 21 receivers and an inline *HED* source, oriented in the profile direction with a minimal offset of 50 m to ensure a good geometrical coverage (Fig. 8). The logarithm of the in-line electric field data was used with 13 frequencies logarithmically spaced from 10^{-2} to 10^4 Hz. The layered inversion grid is composed of 21 layers of increasing thicknesses starting from the first layer below the air interface of 20 m. The inversion grid does not match perfectly the interfaces of the true three layers model used to compute the observed data.

Starting model was chosen as a homogeneous half-space with $\rho_r = 50\,\Omega.\text{m}$. When a CR is considered a low imaginary part is considered in the starting model taking $\rho_q = -0.05\,\Omega.\text{m}$ to obtain a starting phase of $\phi_{\text{cpx}} = -1$ mrad. Data residuals were weighted by a 1 per cent relative error in the covariance matrix (see Appendix B

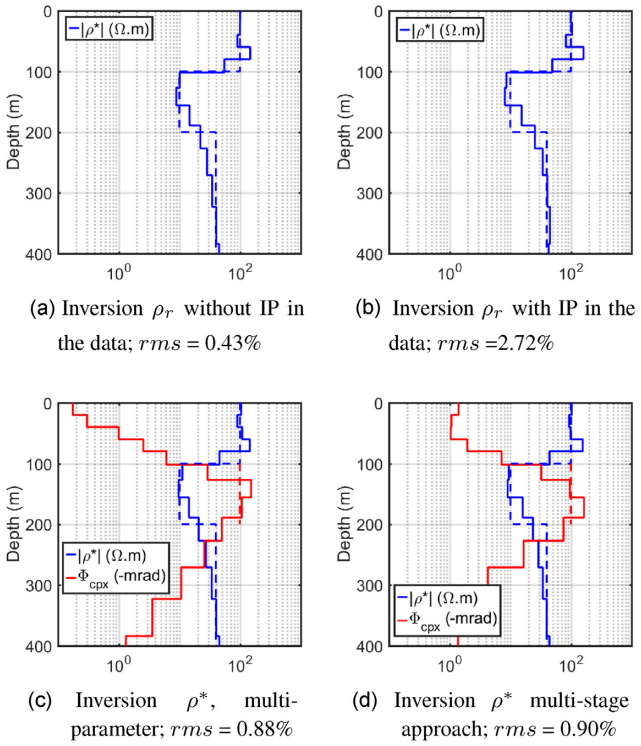

Figure 9. 1-D results for the different inversions considering a real resistivity medium with and without IP in the data, or a CR medium using a multiparameter or a multistage inversion. Blue lines represent the resistivity amplitude (solid, inverted; dashed, true), red lines represent the resistivity phase (solid, inverted; dashed, true).

for covariance and rms estimation). No noise was added in the data. A maximum smoothness regularization was used in the following 1-D examples with a regularization parameter λ equal to 1. We present in Figs 9(a) and (b) the results of the inversion of the real part of the resistivity, for synthetic data generated without and with IP. Then, inversions of CR models are presented searching for the CR norm and phase simultaneously in a multiparameter inversion and then separately through the multistage strategy (Figs 9c and d). The latter inversion uses only electric field amplitude data in the first stage, then during the second stage only the electric field phase data.

The first inversion result (Figs 9a) that seeks a real and constant resistivity model without IP in the data is well resolved with smooth variations with a data rms equal to 0.43 per cent. An acceptable rms is defined as a 1 per cent rms. The second inversion result (Figs 9b) includes IP effects in the data but does not take into account a CR during the inversion. The model is well resolved, nevertheless data rms did not converge more than 2.72 per cent. The remaining residuals are due to the phase of the data that are not well fitted due to IP effects which are not taken into account during the inversion. Multiparameter inversion of the CR resolving simultaneously amplitude and phase of the CR is shown in Fig. 9(c). Data are well fitted with a *rms* of 0.88 per cent and a model close to the true model.

The fourth inversion was performed through the multistage workflow (Fig. 9d). Results are very similar to the multiparameter inversion, but complexities of managing parameters of different classes with different sensitivity were avoided. After the first stage, rms on the data was equal to 2.7 per cent, similarly to the second inversion (Fig. 9b). At the end of the 2nd stage, a satisfactory rms was reached as well, with rms = 0.90 per cent and demonstrating the efficiency of the multistage workflow.

3.2.4 *Frequency dependent complex resistivity parametrization*

Inverting a frequency-dependent CR $\rho^*(\omega)$ is challenging as each frequency multiplies the total number of model parameters. To decrease the total number of parameters, a Cole–Cole parametrization of the CR is commonly used to reduce the unknowns to four parameters per cell. Nevertheless, this parametrization assumes that the resistivity model follows strictly a Cole–Cole relaxation. Let's consider a Cole–Cole model: ρ_0 is the DC resistivity, m the amplitude of the drop from ρ_0 to ρ_∞ at high frequency and the phase peak amplitude, τ the inflexion point of the CR amplitude spectrum and the phase peak position and at last the frequency exponent c that controls the broadness of CR variations with respect to frequency. We already saw that sensitivity to IP effect is reasonably small compared to EM effects and that a part of the IP information will not be accessible. Only a small portion of the residual contains information on the shape of the CR model. We choose to use a 2nd order polynomial support to describe the CR spectrum adapted to a multistaged strategy. Indeed, we obtain thus two independent polynomials to describe the medium, each having different sensitivity to electrical data. As CSEM data are more sensitive to CR norm variation than to the CR phase, the use of a CC model allows to retrieve a CR phase spectrum even if data are not sensitive to it, which could be seen as an advantage but also misleading in cases with low information on the medium and low sensitivity. Looking for two independent polynomials allows to cross-check results between CR norm and phase and to pay more attention to what is reliable in the data. In most cases, 2nd order polynomials are expected to be sufficient to describe the CR model with an acceptable accuracy according to resolution limitation with depth and expected noise at the field scale. It results in six parameters per cell: three for each polynomial, p^n and q^n describing, respectively, $|\rho^*|(\omega)$ and $\phi_{\text{cpx}}(\omega)$. Nevertheless, using the multistaged strategy detailed previously, only three parameters are managed at once, the coefficient of degree zero dealing with a mean constant resistivity and the two coefficients of higher degree related to the frequency dependence shape as the slope and the second-degree curvature of the CR spectrum.

Again, the logarithm of $|\rho^*|(\omega)$ and $\phi_{\text{cpx}}(\omega)$ parameters was chosen for the polynomials description. Furthermore, as resistivity variations with frequency are following a power law with frequency, the logarithm of the frequency was chosen for the polynomial description. Polynomial coefficients used to describe the CR spectrum are then defined by eqs (29) and (30):

$$\log(|\rho^*|) = \sum_{j=0}^{n=2} p_j * \log_{10}(f)^j \tag{29}$$

$$\log(-\phi_{\text{cpx}}) = \sum_{j=0}^{n=2} q_j * \log_{10}(f)^j, \tag{30}$$

with f the frequency. Model vector becomes then:

$$m = \begin{pmatrix} p^0 \\ p^1 \\ p^2 \\ q^0 \\ q^1 \\ q^2 \end{pmatrix} \tag{31}$$

Using the logarithm of the amplitude and phase of the CR, the zeroth-order term corresponds naturally to the value at 1 Hz. In

order, to keep this value in an investigated frequency range, we translate this '*pivot*' frequency to obtain a pivot frequency in the middle of the spectrum investigated.

In the case of the frequency-dependent CR, the gradient can be obtained by directly perturbing each polynomial coefficient parameter or by using a change of variable of $|\rho^*|(\omega)$ and $\phi_{\text{cpx}}(\omega)$ related gradients. The change of variable allows a considerable improvement using 2 calls to forward modelling per data and per layers as for the constant resistivity case, whereas perturbing directly polynomial coefficients needs $2(N_p + 1)$ forward call per data and layers, with N_p the degree of the polynomials. The gradient is obtained using the chain rule. Considering $|\rho^*|(\omega)$ polynomial, we obtain:

$$\left(\frac{\partial \chi}{\partial p_n}\right) = \left(\frac{\partial \log(|\rho^*|(\omega))}{\partial p_n} \frac{\partial \chi}{\partial \log(|\rho^*|(\omega))}\right) \tag{32}$$

It results in sum notation in:

$$\left(\frac{\partial \chi}{\partial p_n}\right) = \sum_{i=1}^{N_{freq}} \log_{10}(f_i)^n \frac{\partial \chi}{\partial \log(|\rho^*|(f_i))} \tag{33}$$

Gradient and Jacobian of ϕ_{cpx} polynomial are obtained using the same method.

As the three coefficients of each polynomial are describing the resistivity norm or the resistivity phase, some crosstalks exist between each parameter of a same polynomial. A preconditioning of the inverse problem is applied by scaling the coefficients of degrees higher than zero in order to adjust their sensitivity. These coefficients are related to the slope and the 2nd order curvature of the spectrum which are ruling our data at the second order compared to the constant components of the CR. The scaling of each coefficient by a constant p_{sc}^n is introduced as a trade-off between parameters, preconditioning in a sense the priority order of each parameter. Indeed, a logical way to lead the inversion to the true resistivity starting from a homogeneous medium is to use a parametrization giving an appropriate weight to polynomial coefficients, solving the main constant component in priority as it explains the data at first order, then an acceptable slope and/or the 2nd order coefficients.

3.2.5 *Polarizable layer model inversion*

Synthetic inversions of a frequency-dependent CR model are presented in the following to illustrate our multiparameter and multistage inversion method. Synthetic survey and model geometry used for the constant CR model inversion were re-used with a frequency-dependent CR conductive layer based on two different Cole–Cole models and presented in Fig. 10. A polynomial is fitted on each curve to provide an idea of the resolution capabilities of 2nd order polynomials compared to a CC model. The chosen CC models are similar with $\rho_0 = 10\,\Omega.\text{m}$, $m = 0.5$ and $c = 0.5$ ensuring a sufficient response with a maximum CR phase above -100 mrad, whereas we chose two different relaxation times in order to play with the inductive coupling response with $\tau_1 = 0.1\,s$ presenting low to medium EM/IP coupling and $\tau_2 = 0.001\,s$ presenting a high coupling between IP and induction responses.

Synthetic data were calculated using the 1-DSA code for the exact three layers model, whereas GN inversions were performed using the polynomial parametrization on a grid of 21 layers similarly to previous examples using a GN optimization. Regularization used was a maximum smoothness constraint with the previous iteration as a reference to ensure smooth variations. Furthermore, the minimum L2-norm deviation from the previous iteration was added here in order to regularize large model updates between iterations. Additional regularization with the minimum norm allows stabilizing

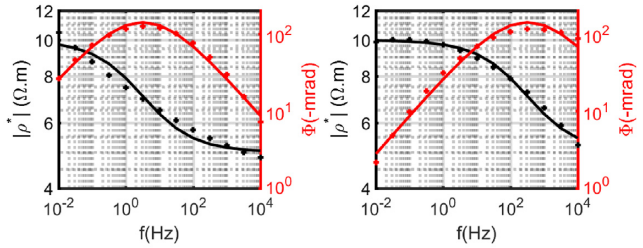

Figure 10. Cole–Cole resistivity models introduced in the conductive layer of the true model for two different relaxation times, $\tau_1 = 0.1\,s$ and $\tau_2 = 0.001\,s$, with $\rho_0 = 10\,\Omega.\text{m}$, $m = 0.5$ and $c = 0.5$; solid lines represent the true model whereas cross markers represent the best polynomial fit using a polynomial of degree 2.

the multiparameter problem as it helps to prevent large steps of one parameter compared to the others.

The starting model is as previously a 50 Ω.m half-space with –1 mrad. Results of the multistaged inversions are shown in Figs 11(a) and (b) for the long τ_1 and the short τ_2 time constant models. The amplitude of the resistivity was solved in the first stage (1), whereas the resistivity phase was solved in the second stage using the model obtained in (1). We used in these examples a scaling p_{sc}^1 and p_{sc}^2 of 0.1 and 0.025 in order to help the trade-off between polynomial parameters of degree zero and $n > 0$.

$|\rho^*|^{\text{inv}}$ results correspond to the first stage of the inversion procedure with an unmodified constant and negligible CR phase set to -1 mrad in the starting model, whereas the CR phase ϕ_{cpx}^{inv} images correspond to the result of the second stage starting from the result of the first stage. τ_1 model had a starting rms of 70.4 per cent, was improved to 2.70 per cent during stage (1) and a final rms of 0.97 per cent was reached after stage (2). Considering τ_2 model, the starting rms was around 64 per cent and was improved in stage (1) to 1.45 per cent and in stage (2) to 0.84 per cent. rms are lower for the short relaxation time layer model, as IP effects are competing with EM induction and due to the loss of sensitivity to the buried layer towards high frequency. Fig. 12 presents an example of the data fit improvement during the multistage procedure for a receiver at the centre of the acquisition profile for τ_1 and τ_2 layer models. Amplitude and phase data of the electric field are very well fitted. Note that at the end of stage (1), amplitude data are perfectly fitted whereas a relatively large residual is remaining on the phase. This phase residual is inverted with success during the stage (2) of our inversion workflow.

During the first stage inverting the electric field amplitude of the data, the geometry of the true medium is correctly solved for both relaxation times as well as the frequency dependence of the CR norm. The top of the polarizable layer is well located whereas the bottom limits of the conductive layer show a smoother transition as the bottom of conductive layers are harder to solve. The soundings show that a correct trend is obtained for both CC relaxation time constants. Fig. 13 shows CR spectra in the polarizable layer for the true, the starting and the inverted models. The second stage allows to retrieve the CR phase by inverting electric field phase data only. The polarizable layer geometry is well resolved on the CR phase. The shapes of the phase spectra are in good agreement with the true CC phase shapes. The CR phase spectra are presented for the layer at 120 m depth in Figs 13(b) and (c). We can see that phase maxima are relatively well retrieved. The lower fit of the phase maxima of Fig. 13(b) comparative to 13(c) can be explain

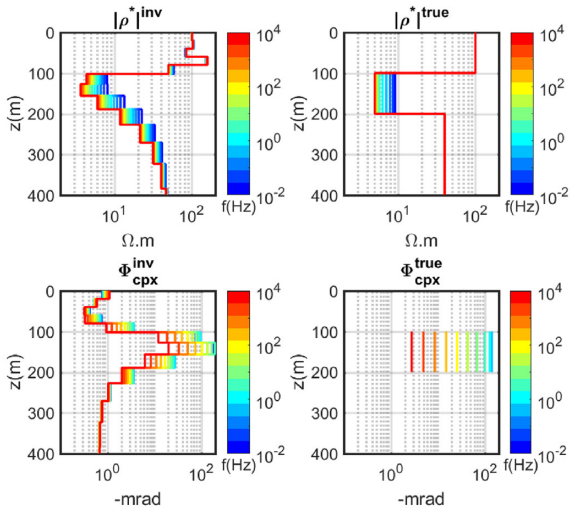

(a) τ_1 CC layer model

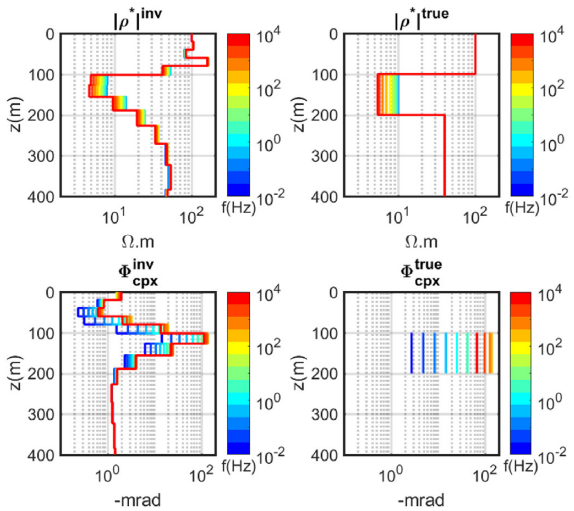

(b) τ_2 CC layer model

Figure 11. Inversion results for the τ_1 and τ_2 CC layer models with, respectively, a low and a high EM/IP coupling using a 500 m profile of 21 receivers and an inline *HED* source as described in Fig. 8. Note that $|\rho^*|^{\text{inv}}$ subplot are the results of stage 1 and are not modified during stage 2, whereas subplot ϕ_{cpx}^{inv} are the results of stage 2 and were kept at the starting model values during stage 1 as only $|\rho^*|$ is inverted.

by some equivalence issues inherent to the method. However, the shapes are not well constrained on their flank where phase values are low despite good data fits (Fig. 12). It can be noticed again that large EM effects can be observed above 2–3 Hz. Whereas a DCIP algorithm is expected to give similar to better results for the τ_1 model below these frequencies (which contains the majority of the IP information) it is obvious that neglecting EM effects for τ_2 model inversion would lead to wrong estimations of the CR as most of the IP information is above 1 Hz and thus perturbed by EM induction.

In this part, we demonstrated that our approach is able of retrieving the geometry of the layer and the shape of the CR spectra for the norm and the CR phase separately. Nevertheless, the bell-shapes of the CR phase spectra are damped where ϕ_{cpx} is low. This is due to a lack of sensitivity to low CR phase (Fig. 3), thus data are less sensitive to these variations during inversion.

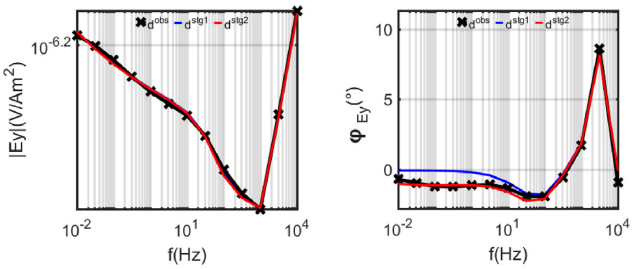

(a) τ_1 model electric field amplitude

(b) τ_1 model electric field phase

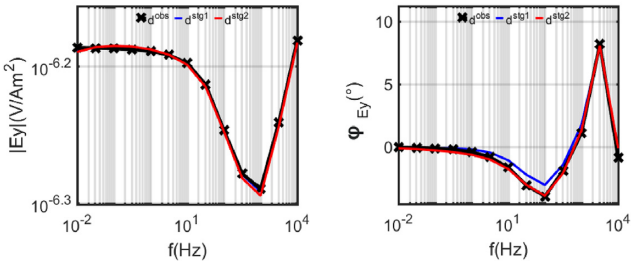

(c) τ_2 model electric field amplitude

(d) τ_2 model electric field phase

Figure 12. Data fit on the in-line electric field amplitude and phase at each stage of the multistage inversion for the τ_1 and τ_2 CC layer models for the receiver at the centre (offset = 300 m) of the profile of 21 receivers (Fig. 8). Black crossed lines are the observed data d^{obs}, blue lines are the data at the end of stage (1) d^{stg1} and red lines are the data at the end of stage (2) d^{stg2}.

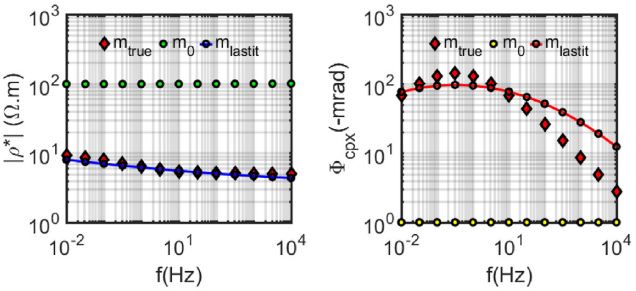

(a) CR norm spectrum for the τ_1 CC layer model at 120 meters depth.

(b) CR phase spectrum for the τ_1 CC layer model at 120 meters depth.

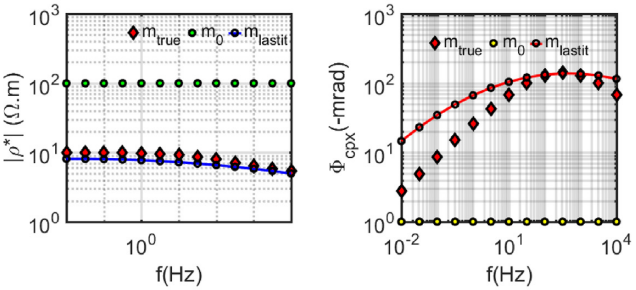

(c) CR norm spectrum for the τ_2 CC layer model at 120 meters depth.

(d) CR phase spectrum for the τ_2 CC layer model at 120 meters depth.

Figure 13. Inversion results for the τ_1 and τ_2 CC layer models with, respectively, a low and a high EM/IP coupling using a 500 m profile of 21 receivers and an inline *HED* source as described in Fig. 8.

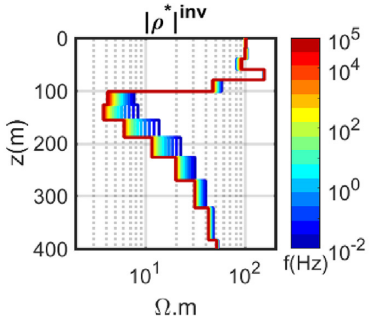

(a) Inversion result with an optimal geometrical illumination. $rms = 1.66$

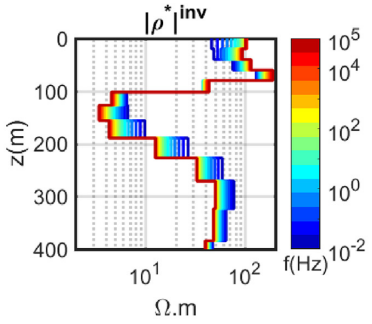

(b) Inversion result with a lack of geometrical information. $rms = 2.43$

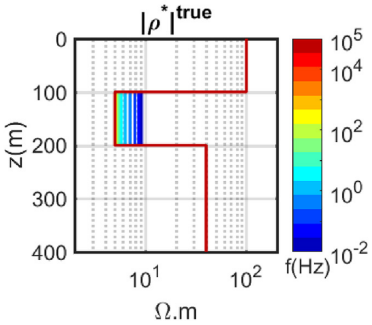

(c) Forwad model

Figure 14. Comparison of the capacity to solve the frequency variation of the CR norm using an optimal frequency sounding acquisition (15 frequencies from 0.01 to 10^5 Hz) and an optimal acquisition geometry (Fig. 8), or using the same receivers geometry but a farther source ($x = 0$ m, $y =$ –500 m) resulting in a lack of geometrical information in the near surface.

3.2.6 Geometrical versus frequency sounding

The previous cases were based on synthetic data sets with an ideal acquisition geometry and investigation frequency window considering the targeted chargeable layer dimension and depth. In CSEM surveys, a part of geometrical information needed in the DC method can be obtained using a frequency sounding, by scanning the medium with the variation of the skin depth and lowering slightly thus the number of TX/RX needed to obtain a correct image. Fig. 14 presents the result of stage (1) for two cases with different geometrical coverages and shows the importance of conserving the maximum of geometrical information to obtain a reliable frequency-dependent CR model. To ensure a perfect frequency sounding even for the shallowest layers of our inverted model, we use in these examples 15 frequencies logarithmically spaced from 10^{-2} to 10^5 Hz, giving a minimal skin depth of 15 m for 100 Ω.m. Fig. 14(a) presents the result for the same acquisition geometry (Fig. 8) as previous 1-D examples for an optimal coverage. On the other hand, Fig. 14(b) presents the inversion result for a farther source with a minimal offset of 500 m. In this way, we introduced a lack of geometrical information close to the surface. We can see that without sufficient geometrical coverage and without additional constraints, the inversion is unable to relocate the frequency variation in the correct layer. Indeed, contrary to classic CSEM methods where the resistivity is considered constant with frequency allowing to constrain the depth of investigation, we have more degrees of freedom and equivalences issues. A sufficient geometrical coverage is thus essential to correctly solve the frequency-varying CR target.

3.3 3-D polarizable cubes inversion

Following 1-D development, the inversion strategy of CR in several stages and based on a second-order polynomial parametrization was adapted to the 3-D case. The gradient computation with respect to the real conductivity of the medium is based on the adjoint state method (Plessix 2006; Plessix & Mulder 2008) described in Appendix A. For the CR case, the gradient is computed for the real $\partial_{\sigma^r}\chi_d$ and the imaginary part $\partial_{\sigma^q}\chi_d$ of the complex conductivity independently at each calculated frequency without additional forward problem resolution using eq. (A17). As the A matrix and the adjoint field λ_e are similar to the real resistivity case. The difference relies only on the differentiation of the system of FD equations A (eq. 9) with respect to σ which contains a term $i\omega\mu$ dependent of σ. The difference between the real and imaginary terms is thus a factor by the imaginary number i and the differentiations with respect to σ^r and σ^q become:

$$\partial_{\sigma^r}\left(A(\sigma^r)E^S - b^*\right)^* = (i\omega\mu)^*\left(E^{S*} + E^{P*}\right) \tag{34}$$

$$\partial_{\sigma^q}\left(A(\sigma^q)E^S - b^*\right)^* = (-\omega\mu)^*\left(E^{S*} + E^{P*}\right) \tag{35}$$

The gradient associated to the polynomial parametrization is then built up from $\partial_{\sigma^r}\chi_d$ and $\partial_{\sigma^q}\chi_d$ using change of variable following the chain rule presented in the 1-D section. Fréchet derivatives are computed using a similar scheme as the gradient, except that a unit residual is back-propagated during the adjoint-state computation for each data separately.

3.3.1 Two-cubes model description

To demonstrate and discuss our frequency dependent CR inversion approach for a 3-D case using a second order polynomial parametrization, synthetic examples are presented for two 3-D targets with different spectral resistivity characteristics. Two cubes of 200 m with different CC properties in a 100 Ω.m homogeneous half-space are investigated. Cubes dimensions and depth are close to the anomaly investigated by Zhdanov *et al.* (2018) without the extension in one horizontal direction. The first cube (cube 1) is a polarizable conductive cube with CC parameters $\rho_0 = 10\,\Omega.\text{m}$, $m = 0.5$, $\tau = 1\,s$, $c = 0.5$, which are close to the parameters of a conductive ore body anomaly presenting an IP response. The cube 1 is centred in $x = 100\,m$, $y = -100\,m$ and $z = 200\,m$. The second cube (cube 2) centred in $x = -100\,m$, $y = 100\,m$ and $z = 200\,m$ was define with CC parameters $\rho_0 = 100\,\Omega.\text{m}$ being equal to the

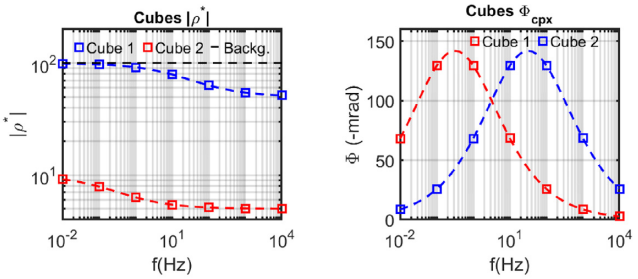

Figure 15. CR spectrum (left-hand panel, norm; right-hand panel, phase) of the Cole–Cole model of cube 1 ($\rho_0 = 10\Omega.\mathrm{m}\, m = 0.5\, \tau = 1s\, c = 0.5$) and cube 2 ($\rho_0 = 100\Omega.\mathrm{m}\, m = 0.5\, \tau = 0.01s\, c = 0.5$).

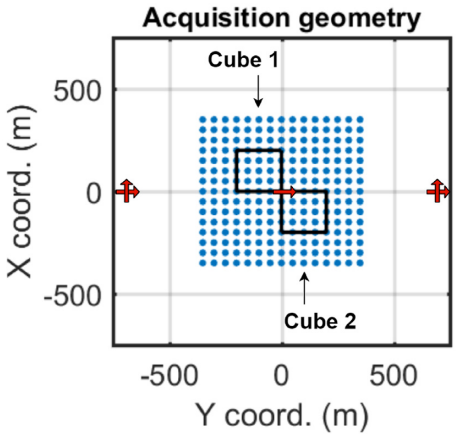

Figure 16. Acquisition geometry using a surface 50×50 m receiver grid (blue dots) above the cubes (cube boundaries projected in surface are represented by black lines) and 5 HED sources (red arrow).

background resistivity, $m = 0.5$, $\tau = 0.01\, s$ and $c = 0.5$ (Fig. 15). These properties were chosen arbitrarily to evaluate the capacity to image a target with low resistivity contrast with the background using only IP effects for the imaging. Two different relaxation times were used with a short and a long τ parameter. At first, each cube models are inverted separately in the homogeneous medium. Models will be referred as *cube 1* model and *cube 2* model, respectively. A third inversion with both cube is then presented.

Acquisition geometry uses a 700×700 meregular receivers grid in surface measuring the electric field in two perpendicular horizontal directions with a 50 m separation in X and Y direction (Fig. 16). Only 5 HED transmitters are used. Transmitters were positioned 700 m on the right and left of the centre of the survey with X-directed and Y-directed polarization to enhance sensitivity of each vertical face of the cubes enhancing horizontal current lines, whereas a fifth HED transmitter Y-oriented was positioned at the centre of the grid to ensure a minimal geometric constraint at short offsets. Considering the central source singularity, data from receivers with offset shorter than 100 m from the transmitter were excluded from the inversion.

3.3.2 Grid description

As the 3-D forward problem results in much higher computational costs than for the 1-D case, we use only seven frequencies from 10^{-2} to 10^{4} Hz in our examples. The forward grid used by the inversion is composed of cells of 12.5×12.5 m horizontally in the core area, from 750 m in both directions in the Y-direction and 400 m in the X-direction as no source is present along this axis. Outside this domain, cells expand progressively to 50×50 m up to 1000 and 750 m, respectively. It allows to keep a sufficiently small cell size in the neighbourhood of the acquisition but reduces the total number of cells as no variation is expected outside the acquisition area for our synthetic example. Vertically, the cells are 3 m thick at the air interface and are expanding by 10 per cent towards depths up to 500 m. Outside this domain, cell sizes increase more abruptly up to a far limit to ensure Dirichlet boundary conditions. A different grid was used for the inversion. Indeed, number of parameters for a classic CSEM inversion is already large and hardly manageable, which becomes worse for the multiparameter problem such as frequency-dependent CR. A coarser 700×700 m grid based on linear splines (De Boor & De Boor 1978) is used for the inversion, with nodes separated by 50 m horizontally in the acquisition area and 5 meters vertically with a 20 per cent expansion rate up to 550 m depth.

Inversion parameters at the boundaries of the inverted domain are vertically extended to the bottom of the forward grid limit, whereas they are extended on 75 m from the horizontal boundaries of the inversion domain. A linear interpolation is applied between the value at the inverted boundaries and the reference model value up to a 250 m distance toward far limits to ensure a smooth transition. The horizontal interpolation distance from the inverted domain is increasing with depth below 250 m depth. It allows avoiding to excessively extend anomalies at the boundaries of the inversion domain outside the inversion domain, where there is no constraint but a sensitivity that can be large.

The resulting grids are a forward model grid around ≈ 500 000 cells and an inversion grid of 4500 spline nodes.

3.3.3 Jacobian scaling

To constrain the large disparity of sensitivity between the central and farther sources and the fast sensitivity decrease beneath receivers to depth, we preconditioned our problem by $\boldsymbol{P_J}$, the inverse of the sum of each line of the Jacobian matrix at the lowest frequency in the reference homogeneous half-space model. We obtain thus a scaling of the model parameters that can be seen as the footprint of the acquisition geometry and compensates for the disparity of sensitivity due to the central transmitter and the fast loss of sensitivity with depth. In order to avoid enhancing excessively areas with no sensitivity, we had limited the scaling by the value at the centre of the acquisition grid, where we are horizontally the most sensitive (below the central transmitter) for a depth of 1/3 the farthest sources offset from the centre of the acquisition grid ($z = 230$ m).

$$\boldsymbol{P}_{\boldsymbol{J_m}} = \frac{1}{(\sum_{j=1}^{N_d} J_{jm}) + \gamma} \quad \text{with } \gamma \text{ a user defined lower limit} \qquad (36)$$

3.3.4 Data

Observed data were modelled with POLYEM3D but using a different forward grid. Cell limits were in accordance with the exact boundaries of the cubes, contrary to the inversion grid. *Wd* covariance matrix contains the inverse of the standard deviation considered as 1 per cent of the total amplitude of the horizontal electric field (see Appendix B). We chose to not introduce a supplementary noise in the observed data of the following examples. However, it can be highlighted that the inverse problem still contains some discrepancies, as there is a numerical noise due to the difference of grid used to solve the observed and calculated data, discrepancies due to the inversion grid using a spline parametrization, or discrepancies between the CC model used to compute the observed data and the

polynomials of 2nd that could fit best the true model. The feasibility in presence of a realistic signal-to-noise ratio is discussed later in the discussion section.

In order to optimize the usable information during the first stage, a slight variation was applied for the 3-D case compared to previous examples. Indeed, we focused previously on amplitude data during the first stage and phase data were ignored at this point as they are affected by the CR phase. We choose to improve the information available by adding a part of the phase data for 3-D model inversion, as polarity information can be essentials in complex geology. Phase data were added during the first stage to improve the EM information used. They were appropriately penalized to avoid taking into account the small phase delay related to ϕ_{cpx}. A covariance representing a relative error of 4 per cent ($\approx 2.3^\circ$) was used.

3.3.5 Stage zero

Synthetic CSEM data were inverted with a GN optimization using LSQR method (Paige & Saunders 1982; Grayver *et al.* 2013) to compute the model perturbation Δm at each iteration. Maximum smoothness regularization was used with a regularization parameter that can be estimated using an L curve. The inversions were undertaken using a remote supercomputing facility part of the French *National Computing Center for Higher Education (CINES)* equipments. Each inversion used 260 cores distributed over 10 nodes of 64 Go and required several tens of hours of computing. No performance test was carried out at the time of these computations as it was not the main goal of this work. However, to provide the reader an estimation of the computational requirements, we needed for the following 3-D examples roughly 40 s to analyse, factorize and solve the FD system of linear equations (eq. 9) and 200 s to compute the Jacobian and the gradient per frequency.

Considering that 3-D problems are more challenging than the 1-D case and that IP effects are small, we started the inversion with a stage '*zero*' prior to stage (1) defined previously to help the local optimization. The starting model is a constant resistivity medium of 100 Ω.m with a negligible CR phase of −1 mrad. In order to get closer to the true medium resistivity before inverting for frequency dependence, stage (0) inverts data to retrieve p^0. p^0 represents a constant resistivity norm medium similarly to a CSEM survey considering a constant and real resistivity. Note that the exponential of the zeroth order polynomial coefficients are presented in the following images in order to correspond to a CR norm [Ω.m] or phase [− mrad] as the polynomials are based on the logarithm of these parameters. Fig. 17 presents the results of stage (0) for the two-cubes and the cube 1 models. No stage (0) inversion was performed for the cube 2 model as there is a low contrast between the background and cube 2, starting model data and synthetic observed data are already close enough. An additional image presents the inversion result of the IP contaminated data of the two-cubes model considering a purely real and constant resistivity inversion and is referred as a '*classical*' CSEM inversion. For this case, no special care on IP contamination was taken to provide a comparison. Inversion iterations were stopped when acceptable *rms* were reached with a convergence rate considered too low. In a real case survey, a user with an experienced eye is needed to understand EM and IP contribution in CSEM data in order to manage these stages by detecting the low IP effect in EM data and having a bigger picture of the capacity to fit the data set according to the situation.

The starting rms for the cube 1 model is 20 per cent, whereas the *rms* of the cube 2 model, with low contrast anomaly is 2 per cent.

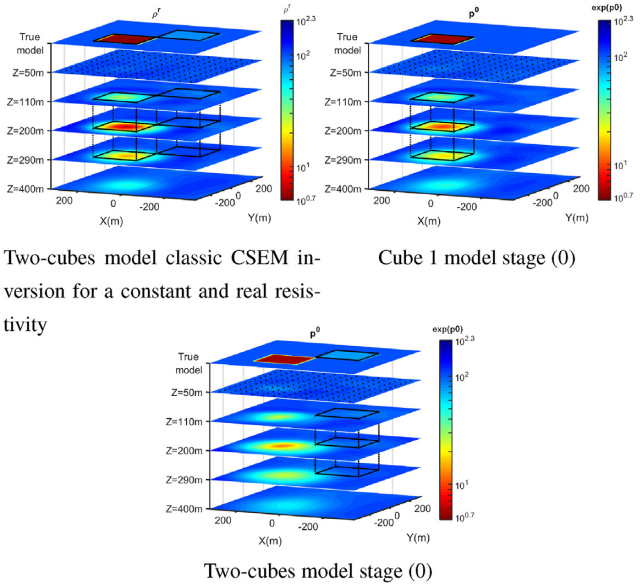

Figure 17. Inversion results for a classic CSEM inversion and stage 0 of two-cubes and cube 1 model. Each plot represents the constant ρ_r (left-hand panel) or the p^0 polynomial parameter for several horizontal slices through the 3-D inverted model at depth $Z = 50$, 110, 200, 290 and 400 m. The first slice represents the corresponding image for the true ρ_r or p^0 model within the cubes (from 100 to 300 m depth). Surface receivers are represented as black dots and projected on the shallowest slice, whereas contours of the cubes are represented as black lines.

The two-cubes model starting rms is about 22 per cent. Each image is close to the true model considering the diffusive limit of CSEM imaging. Cube 1 resistivity is slightly underestimated but well located, with a cube around 10 Ω.*m* in its center. Cube 2 cannot be separated clearly from the background at this stage in Figs 17(a) and (c). Classic CSEM inversion is not severely perturbed by IP effects, nevertheless, data are not perfectly fitted with a remaining rms of 1.33 per cent on amplitude, 0.75 per cent on phase data and a total rms of 1.53 per cent. The remaining total *rms* is already acceptable even without considering IP effects of the target at this depth, which highlights again the necessity of a very low noise data set in order to look for CR spectrum. In the next steps, we applied stage (1) of our inversion workflow. It starts from the model obtained at stage (0) to retrieve the frequency dependence expected in the cubes inverting p^n polynomial coefficients before the consideration of stage (2).

3.3.6 Cube 1 model

At the end of stage 0, inverted data are close to the observed data with a rms = 1.8 per cent. Nevertheless, a slight variation of the amplitude of the measured electric field can be observed as well as a phase due to IP effects. In stage (1), the coefficients of the polynomial describing the norm of the resistivity $|\rho^*|$ are retrieved from the slight variation remaining on electric amplitude data and the weighted phase data. Stage (2) starts then from the model obtained with a 1 per cent covariance on phase data, to fit the phase residual due to the imaginary part of the CR. Stage (2) was directly inverted for the three polynomial coefficients q^n without passing by an intermediate stage solving at first a constant parameter q^0 model.

A regularization parameter equal to 1 was used for stage (1), whereas it was reduced to 0.1 with better results during stage 2. Figs 18(a)–(d) show p^n polynomial coefficients obtained at the end

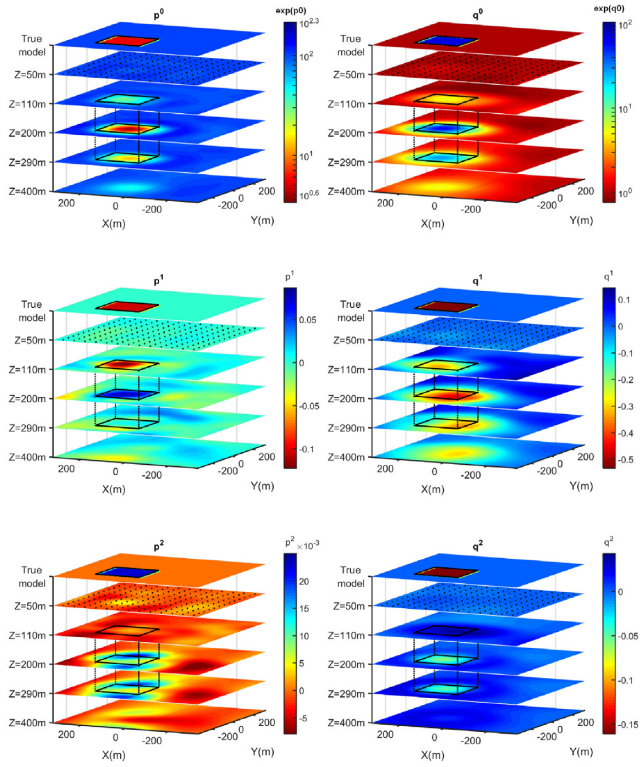

Figure 18. Inversion results for the conductive cube 1 model. Each subplot represents p^n (left-hand panel) or q^n (right-hand panel) from the zeroth to the second degree (top to bottom) polynomial parameters as several horizontal slices through the 3-D inverted model for depth $Z = 50$, 110, 200, 290 and 400 m. The first slice represents the corresponding image for the true model within the cubes (from 100 to 300 m depth). Surface receivers are represented as black dots and projected on the shallowest slice, whereas contours of the cubes are represented as black lines. Individual depth-section slices are provided as online Supporting Information.

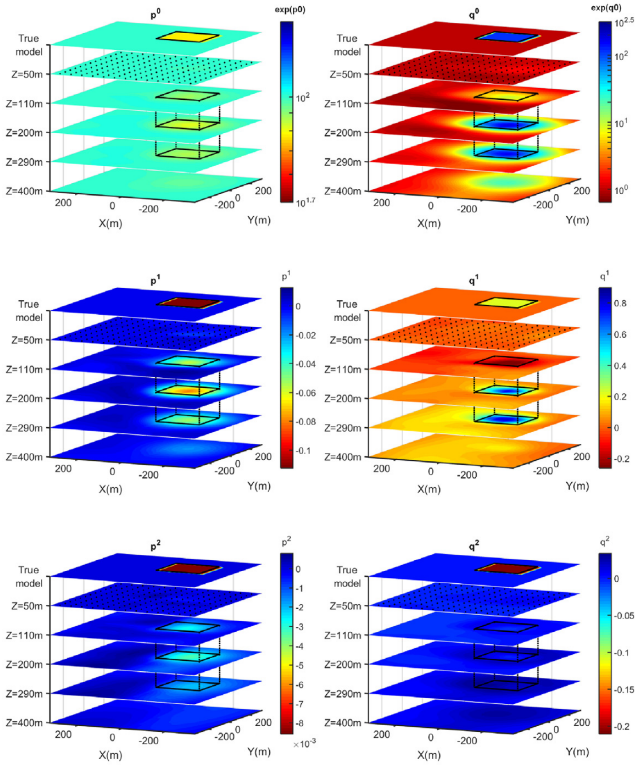

Figure 19. Inversion results for the cube 2 model with low contrast with the background. Each subplot represents p^n (left-hand panel) or q^n (right-hand panel) from the zeroth to the second degree (top to bottom) polynomial parameters as several horizontal slices through the 3-D inverted model for depth $Z = 50$, 110, 200, 290 and 400 m. The first slice represents the corresponding image for the true model within the cubes (from 100 to 300 m depth). Surface receivers are represented as black dots and projected on the shallowest slice, whereas contours of the cubes are represented as black lines. Individual depth-section slices are provided as online Supporting Information.

of stage 1 for the cube 1 model starting from the constant resistivity model of the stage (0). At the end of stage 1 for this model and the followings, data rms is already below 1. As the rms still are locally slightly above 1, in the area above the cube, we thus allowed an overfitting using a covariance with 0.25 per cent of relative error to enhance areas with lower fit with the quadratic norm. Figs 18(b) to (f) present results of the second stage for the q^n polynomial coefficients with a final rms = 0.67 per cent.

Looking at model results at the end of stage 1, we see that our inversion procedure failed to retrieve correctly the frequency dependence of the CR norm of the cube 1 with a perturbed geometry. Several artefacts are seen in the area of cube 1, with a slope p^1 tending to a correct value at the top of the cube but going at lesser extents in the wrong direction below. A similar observation can be made on p^2 value, which tends towards the real value on the edge of the cube only. Stage 2 result (Fig. 18, right-hand plots) presents the q^n polynomial coefficients and shows that even with a low residual remaining to fit, our inversion workflow was able to retrieve the CR phase and a part of the spectral signature of cube 1. The constant CR phase image obtained for the parameter q^0 is very well resolved. A negative slope of the CR phase was retrieved from q^1 image for cube 1. The geometry of the cube is slightly less well resolved as it extends more to depth and slightly overflows its boundaries at $x = 0\,m$ limit. The second-order coefficient q^2 presents a slight anomaly at the cube position in the right direction but its value is largely underestimated and is barely significant.

3.3.7 Cube 2 model

A similar inversion was then undertaken for the cube 2 model, which presents a low contrast with the background medium, but a strong IP response (Fig. 15). This cube has a weak frequency variation of the CR norm below 1 Hz due to the short relaxation time used. IP properties would thus be harder to solve with a static approximation used in the DCIP method, as most of the information is at higher frequencies with an increasing EM coupling. Figs 19(a)–(c), shows p^n polynomial coefficients obtained during the first inversion stage for the cube 2 model and Figs 19(d)–(f) the results of stage (2) with a final $rms = 0.41$ per cent. The p^n polynomial coefficients describing the CR norm of the cube 2 model are well resolved. The geometry of the anomaly fit the dimension of the 3-D cube. p^0 and p^1 values at the center of the cube are in agreement with the true values but slightly underestimated. p^2 value presents an anomaly reflecting the cube dimension, but its value is largely underestimated. Considering q^n polynomial coefficients describing the CR phase of the medium the constant parameter q^0 is well resolved and imaged well the position of the cube. The spectral behaviour parameters are less well resolved. A large and overestimated positive slope q^1

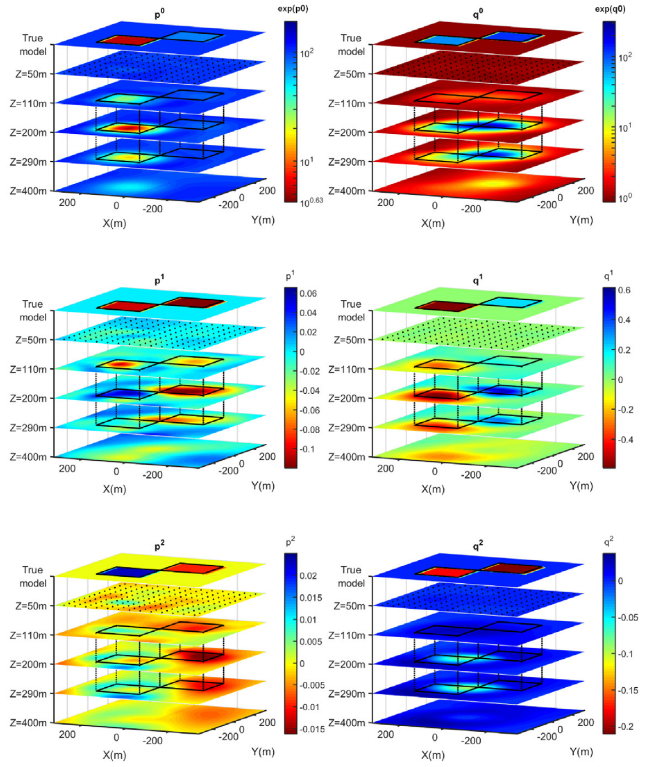

Figure 20. Inversion results for the 'two-cubes' model. Each sub-plot represents p^n (left-hand panel) or q^n (right-hand panel) from the zeroth to the second degree (top to bottom) polynomial parameters as several horizontal slices through the 3-D inverted model for depth $Z = 50$, 110, 200, 290 and 400 m. The first slice represents the corresponding image for the true model within the cubes (from 100 to 300 m depth). Surface receivers are represented as black dots and projected on the shallowest slice, whereas contours of the cubes are represented as black lines. Individual depth-section slices are provided as online Supporting Information.

is obtained at the cube position but no variation of q^2 parameter is imaged.

3.3.8 *Two-cubes model*

In a third inversion, both cubes are inserted into the homogeneous half-space to increase the complexity and determine if previous observations are impacted by interactions between the cubes during the inversion process. Fig. 20 presents both polynomial coefficients results describing the CR of the medium and following the same figure layout as Figs 18 and 19. The final rms at the end of the inversion workflow for the two-cubes model is 0.9 per cent.

Looking at model results at the end of stage 1, we see that the inversion failed to retrieve correctly the spectral signature (p^1 and p^2) of the conductive cube as well as in the cube 1 model inversion. Similar artefacts are observed. Cube 2 polynomial p^n is correctly retrieved. However, notice that with the largest resistivity contrast of the two-cubes model compared to the cube 2 model, cube 2 is not clearly differentiated from the background on the constant p^0 parameter. On the contrary, the parameters describing the CR norm spectral shape are well retrieved and allow to clearly dissociate the cube from the background. Indeed, p^1 and p^2 are negative and in agreement with the true values. p^1 is geometrically well resolved, whereas p^2 is spreading out of the cube boundaries. Stage 2 results present the q^n polynomial coefficients where both cubes are imaged

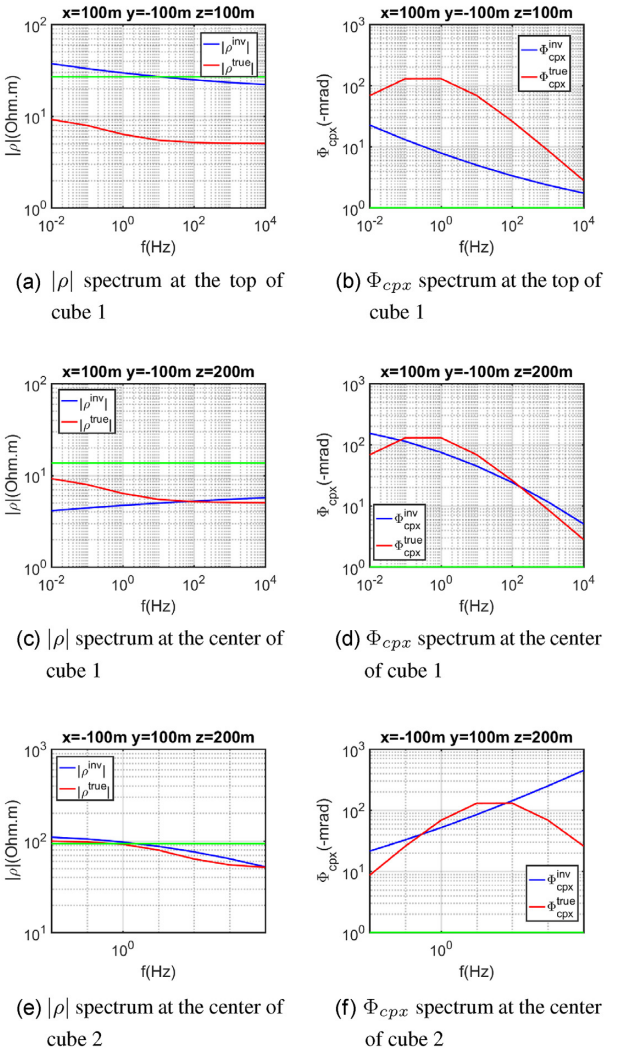

(a) $|\rho|$ spectrum at the top of cube 1
(b) Φ_{cpx} spectrum at the top of cube 1
(c) $|\rho|$ spectrum at the center of cube 1
(d) Φ_{cpx} spectrum at the center of cube 1
(e) $|\rho|$ spectrum at the center of cube 2
(f) Φ_{cpx} spectrum at the center of cube 2

Figure 21. CR spectra at the centre of the cubes and at the top-centre of cube 1 for the two-cubes model. Green curves are the spectrum at the end of previous inversion stage (stage 0 for $|\rho|$ and stage 1 for Φ_{cpx}).

by a unique constant CR phase anomaly. Indeed, cubes are seen as a smooth and elongated q^0 anomaly oriented in the cubes diagonal. However, the CR phase slope q^1 clearly allows the differentiation of both cubes from the background and more importantly between themselves, with two slopes in opposite directions due to the difference in relaxation times. Considering, the last parameter q^2, a slight negative variation can be observed but is not significant again.

Fig. 21 summarized the results of the polynomial coefficients under the form of CR spectra at the centre of the cube positions. The spectra at the top of cube 1 are also displayed as its geometry was not well retrieved. It shows that the cube 1 anomaly at the top-centre (Fig. 21a) of the cube could reflect a coherent CR norm spectral variation contrary to the anomaly retrieved below, at the centre of cube 1 (Fig. 21c). CR norm spectra of cube 2 (Fig. 21e) is in very good agreement with the true model. Considering CR phase spectra both cube results are in good agreement with the major trends of the true CR phase spectral shapes (Figs 21b, d and f). The CR phases of cube 2 (Fig. 21f) are largely overestimated at high frequencies which is explained by the loss of sensitivity due to the skin effect.

4 DISCUSSION

A multistage workflow and a polynomial parametrization were developed and used to constrain the multiparameter inverse problem associated to the inversion of a CR medium taking into account its spectral behaviour. The inversion strategy is based on the relationships observed between the IP effects on the amplitude of the electric field and the CR norm variations and between the IP effects observed on the electric field phase and the CR phase. The proposed strategy solves the CR norm and phase separately during the inversion based thus uniquely on data sensitivity to these parameters. Indeed, both $|\rho^*|(\omega)$ and $\phi_{\text{cpx}}(\omega)$ parts describing the CR are not coupled by a specific model as it is the case for a Cole–Cole model. 1-D synthetic examples demonstrated the efficiency of the method and parametrization. It allowed to retrieve a good CR spectrum shape for the norm and the phase of a buried layer. Nevertheless, even for simple cases using a 1-D model, IP sensitivity issues are already challenging when considering a buried target.

Considering 3-D synthetic examples, the inverse problem is much larger and the IP sensitivity of CSEM data to buried and limited polarizable body is decreasing. Some encouraging results can nevertheless be highlighted here. Cube 2 CR spectrum trend was relatively well retrieved in the cube 2 and two-cubes synthetic models on the norm and the phase. Cube 1 failed to retrieve the correct CR norm spectrum due to equivalence problems. Nevertheless, the constant parameter and the main trend of CR phase spectral variations were correctly retrieved and well located during the second stage for the q^1 parameter. Excepting for the cube 2 CR norm (Fig. 20c) matching relatively well the true p^2 value, the second-order polynomial coefficient was not well imaged in the 3-D case for a target at this depth. In addition to the low sensitivity of IP effects, the limited resolution of the CR spectral shape can be explained partially by the depth of the buried target and the gradual loss of sensitivity of EM data at increasing frequencies, as the skin depth is decreasing. The spectrum shape is thus less well constrained at high frequencies and no more sensitive to these depths. Through our 3-D model, we demonstrated that both cubes could be discriminated from the background in several ways when looking for IP effects. Cube 1 is easily dissociated from the background due to its high conductivity, but also with its constant CR phase parameter q^0. Even though the fact we failed to obtain a correct norm spectrum, we show that a correct CR phase trend could be retrieved from the electric phase residual. On the contrary, the cube 2 anomaly presents a short characteristic time and is very hard to dissociate from the background using only a constant CR norm (or a constant ρ^r), whereas large EM induction perturbations are expected due to the depth of the target and frequency needed to investigate such short relaxation time. Cube 2 results highlight thus the advantages of taking into account the IP effects in CSEM data, where we succeed to retrieve the CR norm variation from the constant background. Considering the CR phase, the constant parameter q^0 allows the dissociation of the second cube from the background as well, but also using its spectral behaviour. Finally, the spectral behaviour of both cubes could also clearly be differentiated between themselves using the opposed slope q^1 observed on the CR phase. The resulting slopes on the CR phase let us differentiate between the long and the short relaxation time anomaly.

We saw that CSEM data sensitivity to IP effects of deep 3-D targets is relatively weak even considering a large frequency-dependent CR anomaly (high chargeability, CR phase peak below −100 mrad). The IP signal gets close to numerical accuracy as the depth of the target increases and its size decreases. In our examples, we did not consider an additional noise. The presence of noise would certainly affect our capacity to retrieve correctly a CR medium and its frequency dependence depending on the measurement quality and the case-dependent cultural noise. Therefore, data with an exceptional signal-to-noise ratio are necessary to expect to retrieve such results in the case of a real survey. However, it is possible to improve the signal-to-noise ratio by using proper data processing techniques as robust processing algorithms (Egbert & Booker 1986; Streich *et al.* 2013). Furthermore, signal-to-noise ratio can be improved by increasing the source moment. It can be achieved by injecting a larger current by using a strong transmitter able to inject several dozen of amperes (Streich *et al.* 2013; Mörbe *et al.* 2020) and/or by increasing injection or receiver dipole sizes as cable-layout responses can be taken into account in the computation of EM fields. Great care should be taken for the positioning of the survey arrays. The positions of electrodes and wire layouts should be measured using a differential GPS positioning system able to reach a centimetric accuracy. A repeatability error around 0.1 per cent can thus be reached as demonstrated in Darnet *et al.* (2020) for a time-lapse land-CSEM application at a kilometric scale. In their repeatability study. Tietze *et al.* (2019) showed that they could reach an accuracy within the range of ≈0.1–0.3 per cent relative to the measured field amplitude for source–receiver offsets below 2 km. Despite being quite challenging, we thus consider that a sufficiently good accuracy is reachable as IP studies are restricted to near-surface investigations due to the fast loss of sensitivity inherent to IP phenomena.

An acceptable constant real resistivity model of the 3-D buried targets was retrieved during the inversion of CSEM data contaminated by IP effects without taking a frequency-dependent CR into account (Fig. 17). However, we showed that by using an appropriate parametrization and a pragmatic workflow, we were able to better explain the data and retrieve successfully a significant part of the IP information for these deep targets as well as taking EM induction into account in the imaging process.

Considering shallower targets, larger IP effects would be expected in EM data, but the choice of the imaging method should be cautiously considered between DCIP and CSEMIP. Indeed, the need of a numerically expensive CSEMIP inversion instead of using the DC assumption should be carefully evaluated according to the EM information expected in the data. Indeed, as the polarizable target is getting shallower, shorter offsets can be used for the imaging problem and thus data are gradually less subject to EM contamination in IP data. However, they contain also less EM information that could help for the reconstruction of the medium. While the DC method can offer a better resolution in shallow subsurface due to the use of a larger number of TX-RX arrays combined with a lighter computational requirement compared to CSEM methods, it can require a larger logistic as information is obtained geometrically only. On the contrary, adding frequency-sounding information can slightly reduce efforts on the field with a certain complementarity between offset and frequency. Indeed, we image relatively well our cubes with only 5 transmitters in our examples by considering EM effects during the inversion. However, if frequency-sounding information used in EM surveys can lighten the acquisition, the IP problem still requires a sufficient geometrical constraint to solve the CR spectral behaviour due to the underdetermined inverse problem. Otherwise, some artefacts can easily appear as in the reconstruction of the cube 1 polynomial coefficients p^n, which points out that a few supplementary sources could be preferred. Nevertheless, adding supplementary sources would also be computationally more expensive. IP effect is not enough sensitive for these offsets and target depths to be really quantitative without additional constraint

on the target. However, the CSEMIP method still allows the discrimination between the targets spectral signatures and offers thus a supplementary mean of characterization.

5 CONCLUSION

In this work, we successfully managed to implement a frequency-dependent CR into a 3-D CSEM modelling and inversion code. Following a straightforward implementation in the frequency domain CSEM forward problem, the multiparameter inverse problem was decomposed in two main stages based on electric field sensitivity to the norm and phase of the CR and using a second-order polynomial parametrization. Our approach does not rely on a particular empirical IP model. The method was developed and tested on simple 1-D synthetic problems, before an application on 3-D synthetic examples with two different deep targets of interest, a conductive and polarizable cube and a polarizable cube with none of few resistivity contrast with the background. Recovered spectral shapes are imperfect due to the low sensitivity to IP effects of deep-buried targets and some equivalence problems intervening for the CR norm variation of one of the targets taken in our examples. Nevertheless, using our multistage workflow coupled with a polynomial parametrization of the CR allows us to retrieve an important part of the CR spectral trends of the 3-D anomalies considered. CSEMIP method shows a great potential to discriminate between polarizable bodies at large depths and considering simultaneously EM induction information. The spectral behaviours should be sufficiently contrasted for a discrimination of deep target spectral signatures. The CSEMIP problem would require a data set of high quality to access to weak IP effect contained in EM data and implies the use of a forward problem solver of sufficient accuracy. In the future, the implementation of a more specific IP parametrization could be considered for comparison with the polynomial parametrization.

ACKNOWLEDGMENTS

The research and developments leading to these results have received fundings from the French National Research Agency (ANR) in the framework of the project EXCITING (ANR-17-CE06-0012). Large scale 3-D EM modelling and inversion were performed with BRGM's POLYEM3D code using the Occigen supercomputer thanks to GENCI (Grand Equipement de Calcul Intensif) and CINES (Centre Informatique National de l'enseignement Supérieur) supercomputing facilities. We are grateful to the reviewers, M. Bücker, W. Agudelo and an additional *anonymous reviewer*, for their valuable comments which allow us to improve this manuscript.

DATA AVAILABILITY

Restrictions apply to the availability of the code used in this study. The code is however available from the authors upon reasonable request and with permission of the French Geological Survey.

REFERENCES

Amestoy, P., Duff, I.S., Koster, J. & L'Excellent, J.-Y., 2001. A fully asynchronous multifrontal solver using distributed dynamic scheduling, *SIAM J. Matrix Anal. Appl.,* **23**(1), 15–41.

Amestoy, P., Buttari, A., L'Excellent, J.-Y. & Mary, T., 2019. Performance and scalability of the block low-rank multifrontal factorization on multicore architectures, *ACM Trans. Math. Software,* **45**(2), 1–2:26.

Archie, G.E., 1942. The electrical resistivity log as an aid in determining some reservoir characteristics, *Trans. AIME,* **146**(01), 54–62.

Bretaudeau, F., Dubois, F., Bissavetsy Kassa, S., Coppo, N., Wawrzyniak, P. & Darnet, M., 2021. Time-lapse resistivity imaging: CSEM-data 3-D double-difference inversion and application to the Reykjanes geothermal field, *Geophys. J. Int.,* **226**(3), 1764–1782.

Börner, F.D., Schopper, J.R. & Weller, A., 1996. Evaluation of transport and storage properties in the soil and groundwater zone from induced polarization measurements1, *Geophys. Prospect.,* **44**(4), 583–601.

Busch, S., van der Kruk, J., Bikowski, J. & Vereecken, H., 2012. Quantitative conductivity and permittivity estimation using full-waveform inversion of on-ground GPR data, *Geophysics,* **77**(6), H79–H91.

Chave, A.D. & Jones, A.G., 2012. *The Magnetotelluric Method: Theory and Practice,* Cambridge Univ. Press.

Cole, K.S. & Cole, R.H., 1941. Dispersion and absorption in dielectrics I. Alternating current characteristics, *J. Chem. Phys.,* **9**(4), 341–351.

Commer, M., Newman, G.A., Williams, K.H. & Hubbard, S.S., 2011. 3D induced-polarization data inversion for complex resistivity, *Geophysics,* **76**(3), F157–F171.

Constable, S., 2010. Ten years of marine CSEM for hydrocarbon exploration, *Geophysics,* **75**(5), 75A67–75A81.

Darnet, M., Wawrzyniak, P., Coppo, N., Nielsson, S., Schill, E. & Fridleifsson, G., 2020. Monitoring geothermal reservoir developments with the controlled-source electro-magnetic method—a calibration study on the Reykjanes geothermal field, *J. Volc. Geotherm. Res.,* **391,** doi:10.1016/j.jvolgeores.2018.08.015.

Davydycheva, S., Rykhlinski, N. & Legeido, P., 2006. Electrical-prospecting method for hydrocarbon search using the induced-polarization effect, *Geophysics,* **71**(4), G179–G189.

De Boor, C. & De Boor, C., 1978. *A Practical Guide to Splines,* Vol. **27,** Springer-Verlag New York.

Dias, C.A., 2000. Developments in a model to describe low-frequency electrical polarization of rocks, *Geophysics,* **65**(2), 437–451.

Egbert, G.D. & Booker, J.R., 1986. Robust estimation of geomagnetic transfer functions, *Geophys. J. Int.,* **87**(1), 173–194.

Fiandaca, G., Madsen, L.M. & Maurya, P.K., 2018. Re-parameterisations of the Cole–Cole model for improved spectral inversion of induced polarization data, *Near Surf. Geophys.,* **16**(4), 385–399.

García-Fiscal, S. & Flores, C., 2018. Sensitivity of galvanic and inductive induced polarization methods to the Cole-Cole parameters, *J. appl. Geophys.,* **158,** 1–10.

Ghorbani, A., Cosenza, P., Revil, A., Zamora, M., Schmutz, M., Florsch, N. & Jougnot, D., 2009. Non-invasive monitoring of water content and textural changes in clay-rocks using spectral induced polarization: a laboratory investigation, *Appl. Clay Sci.,* **43**(3–4), 493–502.

Grayver, A.V., Streich, R. & Ritter, O., 2013. Three-dimensional parallel distributed inversion of CSEM data using a direct forward solver, *Geophys. J. Int.,* **193**(3), 1432–1446.

Gupta, A., 2000. WSMP: Watson Sparse Matrix Package Part I - direct solution of symmetric sparse systems, IBM TJ Watson Research Center, Yorktown Heights, NY, Tech. Rep. RC 21886.

Karaoulis, M., Revil, A., Werkema, D., Minsley, B., Woodruff, W. & Kemna, A., 2011. Time-lapse three-dimensional inversion of complex conductivity data using an active time constrained (atc) approach, *Geophys. J. Int.,* **187**(1), 237–251.

Kemna, A. *et al.*, 2012. An overview of the spectral induced polarization method for near-surface applications, *Near Surf. Geophys.,* **10**(6), 453–468.

Kessouri, P. *et al.*, 2019. Induced polarization applied to biogeophysics: recent advances and future prospects, *Near Surf. Geophys.,* **17**(6), 595–621.

Kim, H.J., Song, Y. & Lee, K.H., 1997. High-frequency electromagnetic inversion for a dispersive layered earth, *J. Geomagnet. Geoelectr.,* **49**(11–12), 1439–1450.

Lavoué, F., Brossier, R., Métivier, L., Garambois, S. & Virieux, J., 2014. Two-dimensional permittivity and conductivity imaging by full waveform inversion of multioffset GPR data: a frequency-domain quasi-Newton approach, *Geophys. J. Int.,* **197**(1), 248–268.

Liu, M., Yang, J., Feng, J., Wang, T. & Zhang, H., 2016. A discussion on the performance of seven existing models proposed to describe induced polarization IP models and analog computation, *Geophysics,* **81**(6), E459–E469.

MacLennan, K., Karaoulis, M. & Revil, A., 2014. Complex conductivity tomography using low-frequency crosswell electromagnetic data, *Geophysics,* **79**(1), E23–E38.

Madden, T.R. & Cantwell, T., 1967. Part D. Induced polarization, a review, in *Mining Geophysics,* Vol. II, Theory, pp. 373–400, Society of Exploration Geophysicists.

Martin, T., Günther, T., Orozco, A.F. & Dahlin, T., 2020. Evaluation of spectral induced polarization field measurements in time and frequency domain, *J. appl. Geophys.,* **180,** doi:10.1016/j.jappgeo.2020.104141.

Métivier, L. & Brossier, R., 2016. The seiscope optimization toolbox: a large-scale nonlinear optimization library based on reverse communication the seiscope optimization toolbox, *Geophysics,* **81**(2), F1–F15.

Mörbe, W., Yogeshwar, P., Tezkan, B. & Hanstein, T., 2020. Deep exploration using long-offset transient electromagnetics: interpretation of field data in time and frequency domain, *Geophys. Prospect.,* **68**(6), 1980–1998.

Newman, G.A. & Alumbaugh, D.L., 1995. Frequency-domain modelling of airborne electromagnetic responses using staggered finite differences, *Geophys. Prospect.,* **43**(8), 1021–1042.

Nocedal, J. & Wright, S., 2006. *Numerical Optimization,* Springer Science & Business Media.

Orozco, A.F., Kemna, A., Oberdörster, C., Zschornack, L., Leven, C., Dietrich, P. & Weiss, H., 2012. Delineation of subsurface hydrocarbon contamination at a former hydrogenation plant using spectral induced polarization imaging, *J. Contam. Hydrol.,* **136,** 131–144.

Paige, C.C. & Saunders, M.A., 1982. ALGORITHM 583: LSQR: sparse linear equations and least squares problems, *ACM Trans. Math. Software (TOMS),* **8**(2), 195–209.

Palacky, G., 1988. Resistivity characteristics of geologic targets, *Electromagnet. Methods Appl. Geophys.,* **1,** 53–129.

Pelton, W.H., Ward, S.H., Hallof, P.G., Sill, W.R. & Nelson, P.H., 1978. Mineral discrimination and removal of inductive coupling with multifrequency IP, *Geophysics,* **43**(3), 588–609.

Plessix, R.-E., 2006. A review of the adjoint-state method for computing the gradient of a functional with geophysical applications, *Geophys. J. Int.,* **167**(2), 495–503.

Plessix, R.-E. & Mulder, W., 2008. Resistivity imaging with controlled-source electromagnetic data: depth and data weighting, *Inverse Problems,* **24**(3), doi:10.1088/0266-5611/24/3/034012.

Qi, Y., El-Kaliouby, H., Revil, A., Soueid Ahmed, A., Ghorbani, A. & Li, J., 2019. Three-dimensional modeling of frequency-and time-domain electromagnetic methods with induced polarization effects, *Comput. Geosci.,* **124,** 85–92.

Routh, P.S. & Oldenburg, D.W., 2001. Electromagnetic coupling in frequency-domain induced polarization data: a method for removal, *Geophys. J. Int.,* **145**(1), 59–76.

Seigel, H.O., 1959. Mathematical formulation and type curves for induced polarization, *Geophysics,* **24**(3), 547–565.

Shantsev, D.V. & Maaø, F.A., 2015. Rigorous interpolation near tilted interfaces in 3-D finite-difference EM modelling, *Geophys. J. Int.,* **200**(2), 745–757.

Spies, B.R. & Frischknecht, F.C., 1991. Electromagnetic sounding, *Electromagnet. Methods Appl. Geophys.,* **2**(Part A), 285–426.

Streich, R., 2009. 3D finite-difference frequency-domain modeling of controlled-source electromagnetic data: direct solution and optimization for high accuracy, *Geophysics,* **74**(5), F95–F105.

Streich, R., Becken, M. & Ritter, O., 2013. Robust processing of noisy land-based controlled-source electromagnetic data, *Geophysics,* **78**(5), E237–E247.

Tietze, K., Ritter, O., Patzer, C., Veeken, P. & Dillen, M., 2019. Repeatability of land-based controlled-source electromagnetic measurements in industrialized areas and including vertical electric fields, *Geophys. J. Int.,* **218**(3), 1552–1571.

Vanhala, H., 1997. Mapping oil-contaminated sand and till with the spectral induced polarization (SIP) method, *Geophys. Prospect.,* **45**(2), 303–326.

Veeken, P.C., Legeydo, P.J., Davidenko, Y.A., Kudryavceva, E.O., Ivanov, S.A. & Chuvaev, A., 2009. Benefits of the induced polarization geoelectric method to hydrocarbon exploration, *Geophysics,* **74**(2), B47–B59.

Virieux, J. & Operto, S., 2009. An overview of full-waveform inversion in exploration geophysics, *Geophysics,* **74**(6), WCC1–WCC26.

Waxman, M.H. & Smits, L., 1968. Electrical conductivities in oil-bearing Shaly sands, *Soc. Petrol. Eng. J.,* **8**(02), 107–122.

Zhdanov, M., 2008. Generalized effective-medium theory of induced polarization, *Geophysics,* **73**(5), F197–F211.

Zhdanov, M., Endo, M., Cox, L. & Sunwall, D., 2018. Effective-medium inversion of induced polarization data for mineral exploration and mineral discrimination: case study for the copper deposit in Mongolia, *Minerals,* **8**(2), 68, doi:10.3390/min8020068.

Xu, Z. & Zhdanov, M.S., 2015. Three-dimensional Cole-Cole model inversion of induced polarization data based on regularized conjugate gradient method, *IEEE Geosci. Remote Sens. Lett.,* **12**(6), 1180–1184.

Zonge, K.L. & Hughes, L.J., 1991. Controlled source audio-frequency magnetotellurics, in *Electromagnetic Methods in Applied Geophysics,* Vol. 2, Application, Parts A and B, pp. 713–810, ed. Nabighian, M. N., Society of Exploration Geophysicists.

SUPPORTING INFORMATION

Supplementary data are available at *GJI* online.

Figure S1. Inversion results of the 'two-cubes' model for p^0 the zeroth order polynomial coefficient describing $|\rho^*|(\omega)$. Each slice represent a depth-section at $Z = 50$, 110, 200, 290 or 400 m equivalent to the 3-D view displayed in Fig. 20. The true model depth section is represented (top-left) at the cubes depths.

Figure S2. Inversion results of the 'two-cubes' model for p^1 the first order polynomial coefficient describing $|\rho^*|(\omega)$. Each slice represent a depth-section at $Z = 50$, 110, 200, 290 or 400 m equivalent to the 3-D view displayed in Fig. 20. The true model depth section is represented (top-left) at the cubes depths.

Figure S3. Inversion results of the 'two-cubes' model for p^2 the second order polynomial coefficient describing $|\rho^*|(\omega)$. Each slice represent a depth-section at $Z = 50$, 110, 200, 290 or 400 m equivalent to the 3-D view displayed in Fig. 20. The true model depth section is represented (top-left) at the cubes depths.

Figure S4. Inversion results of the 'two-cubes' model for q^0 the zeroth order polynomial coefficient describing $-\phi(\omega)$. Each slice represent a depth-section at $Z = 50$, 110, 200, 290 or 400 m equivalent to the 3-D view displayed in Fig. 20. The true model depth section is represented (top-left) at the cubes depths.

Figure S5. Inversion results of the 'two-cubes' model for q^1 the first order polynomial coefficient describing $-\phi(\omega)$. Each slice represent a depth-section at $Z = 50$, 110, 200, 290 or 400 m equivalent to the 3-D view displayed in Fig. 20. The true model depth section is represented (top-left) at the cubes depths.

Figure S6. Inversion results of the 'two-cubes' model for q^2 the second order polynomial coefficient describing $-\phi(\omega)$. Each slice represent a depth-section at $Z = 50$, 110, 200, 290 or 400 m equivalent to the 3-D view displayed in Fig. 20. The true model depth section is represented (top-left) at the cubes depths.

Figure S7. Inversion results of the cube 1 model for p^0 the zeroth order polynomial coefficient describing $|\rho^*|(\omega)$. Each slice repre-

sent a depth-section at $Z = 50$, 110, 200, 290 or 400 m equivalent to the 3-D view displayed in Fig. 18. The true model depth section is represented (top-left) at the cubes depths.

Figure S8. Inversion results of the cube 1 model for p^1 the first order polynomial coefficient describing $|\rho^*|(\omega)$. Each slice represent a depth-section at $Z = 50$, 110, 200, 290 or 400 m equivalent to the 3-D view displayed in Fig. 18. The true model depth section is represented (top-left) at the cubes depths.

Figure S9. Inversion results of the cube 1 model for p^2 the second order polynomial coefficient describing $|\rho^*|(\omega)$. Each slice represent a depth-section at $Z = 50$, 110, 200, 290 or 400 m equivalent to the 3-D view displayed in Fig. 18. The true model depth section is represented (top-left) at the cubes depths.

Figure S10. Inversion results of the cube 1 model for q^0 the zeroth order polynomial coefficient describing $-\phi(\omega)$. Each slice represent a depth-section at $Z = 50$, 110, 200, 290 or 400 m equivalent to the 3-D view displayed in Fig. 18. The true model depth section is represented (top-left) at the cubes depths.

Figure S11. Inversion results of the cube 1 model for q^1 the first order polynomial coefficient describing $-\phi(\omega)$. Each slice represent a depth-section at $Z = 50$, 110, 200, 290 or 400 m equivalent to the 3-D view displayed in Fig. 18. The true model depth section is represented (top-left) at the cubes depths.

Figure S12. Inversion results of the cube 1 model for q^2 the second order polynomial coefficient describing $-\phi(\omega)$. Each slice represent a depth-section at $Z = 50$, 110, 200, 290 or 400 m equivalent to the 3-D view displayed in Fig. 18. The true model depth section is represented (top-left) at the cubes depths.

Figure S13. Inversion results of the cube 2 model for p^0 the zeroth order polynomial coefficient describing $|\rho^*|(\omega)$. Each slice represent a depth-section at $Z = 50$, 110, 200, 290 or 400 m equivalent to the 3-D view displayed in Fig. 19. The true model depth section is represented (top-left) at the cubes depths.

Figure S14. Inversion results of the cube 2 model for p^1 the first order polynomial coefficient describing $|\rho^*|(\omega)$. Each slice represent a depth-section at $Z = 50$, 110, 200, 290 or 400 m equivalent to the 3-D view displayed in Fig. 19. The true model depth section is represented (top-left) at the cubes depths.

Figure S15. Inversion results of the cube 2 model for p^2 the second order polynomial coefficient describing $|\rho^*|(\omega)$. Each slice represent a depth-section at $Z = 50$, 110, 200, 290 or 400 m equivalent to the 3-D view displayed in Fig. 19. The true model depth section is represented (top-left) at the cubes depths.

Figure S16. Inversion results of the cube 2 model for q^0 the zeroth order polynomial coefficient describing $-\phi(\omega)$. Each slice represent a depth-section at $Z = 50$, 110, 200, 290 or 400 m equivalent to the 3-D view displayed in Fig. 19. The true model depth section is represented (top-left) at the cubes depths.

Figure S17. Inversion results of the cube 2 model for q^1 the first order polynomial coefficient describing $-\phi(\omega)$. Each slice represent a depth-section at $Z = 50$, 110, 200, 290 or 400 m equivalent to the 3-D view displayed in Fig. 19. The true model depth section is represented (top-left) at the cubes depths.

Figure S18. Inversion results of the cube 2 model for q^2 the second order polynomial coefficient describing $-\phi(\omega)$. Each slice represent a depth-section at $Z = 50$, 110, 200, 290 or 400 m equivalent to the 3-D view displayed in Fig. 19. The true model depth section is represented (top-left) at the cubes depths.

Please note: Oxford University Press is not responsible for the content or functionality of any supporting materials supplied by the authors. Any queries (other than missing material) should be directed to the corresponding author for the paper.

APPENDIX A: ADJOINT STATE METHOD APPLIED TO FD CSEM SCHEME

The gradient computation using the adjoint state method, is summarized in the following after the recipe proposed by Plessix (2006).

State equations

At first, a list of the *state equations* must be established, which are the equations describing the forward problem, as well as the link towards the inversion domain. The state functions are associated with independent state variables. Three state functions can be derived from the forward problem and from forward to inverse domain operators:

(i) The forward problem system, defined as:

$$A(\sigma)E^S = b^S \qquad \text{with} \quad b^S = -i\omega\left(\sigma - \sigma^P\right)E^P, \tag{A1}$$

with $A(\sigma)$ the system of FD equation defined by eq. (9) and developed in appendix in Streich (2009). σ is the conductivity vector defined for each cell of the forward grid.

(ii) The interpolation operator Q, relating the field calculated on the forward staggered grid to data measured at the exact receiver position (Q includes the vector field reorientation, the type of field extracted, etc.). Each data recording at a receiver position is considered as an independent data.

$$QE^S = d_{\text{cal}} \tag{A2}$$

(iii) The operator $C(\sigma)$ that linked the forward to the inverted parameter m, which contains the change of variable and the change of grid operators, defined as:

$$C(\sigma) = m \tag{A3}$$

Three state variables are obtained and will be associated to an *adjoint state* variable of same dimension:

State function	State variable	Adjoint variable
$A(\sigma)E^S = b^S$	E^S	λ_e
$QE^S = d_{\text{cal}}$	d_{cal}	λ_d
$C(\sigma) = m$	σ	λ_σ

Augmented functional $\mathcal{L}$ recipe

(i)At first, the augmented functional (or associated Lagrangian) $\mathcal{L}$ defining the adjoint state problem introducing the objective function, can be defined following Plessix (2006) as:

$$\begin{aligned}\mathcal{L}(m, \sigma, d_{\text{cal}}, E^S, \lambda_\sigma, \lambda_d, \lambda_e) = \chi(d^{\text{cal}}) \quad &- <\lambda_\sigma, C(\sigma) - m> \\ &- <\lambda_d, QE^S - d_{\text{cal}}> \\ &- <\lambda_e, A(\sigma)E^S - b^s>,\end{aligned} \tag{A4}$$

with $<,>$ representing the scalar product notation. The problem of the adjoint state method seeks therefore a solution that minimizes thus the objective function with respect of m, under the constraints of each state function.

(ii)The adjoint state equations are then derived looking for the saddle points of $\mathcal{L}$ with respect to each state variable defined previously. The state variables and the adjoint state variables are considered independent of m.

(a) $\frac{\partial \mathcal{L}}{\partial \mathbf{d}_{\text{cal}}} = \mathbf{0}$

$$\begin{aligned}\frac{\partial \mathcal{L}}{\partial d_{\text{cal}}} &= \partial_d \chi(d^{\text{cal}}) - \partial_d < \lambda_d, QE^S - d_{\text{cal}} > \\ 0 &= (d_{\text{cal}} - d_{\text{obs}}) + \lambda_d \\ \lambda_d &= -\Delta d \end{aligned} \tag{A5}$$

A first adjoint state equation is obtained, which allows to determine the adjoint state variable λ_d that corresponds simply to the residual vector:

$$\boxed{\lambda_d = -\Delta d} \tag{A6}$$

(b) $\frac{\partial \mathcal{L}}{\partial \mathbf{E^S}} = \mathbf{0}$

$$\begin{aligned}\frac{\partial \mathcal{L}}{\partial E^s} &= -\partial_e < \lambda_e, A(\sigma)E^S - b^s > -\partial_e < \lambda_d, QE^S - d_{\text{cal}} > \\ 0 &= -(Q)^t \lambda_d - A(\sigma)^\dagger \lambda_e \\ A(\sigma)^\dagger \lambda_e &= (Q)^t \Delta d \end{aligned} \tag{A7}$$

The second adjoint state relation is a linear system '$Ax = b$', that can be solved to get the adjoint field λ_e by back-propagating the residual on the grid equivalently to a source term. The matrix A is the same as the forward problem and is already factorized, thus a similar form can be used taking the conjugate (noted $\overline{\ }$) of the previous relationship to preserve the A matrix:

$$\boxed{A(\sigma)\overline{\lambda_e} = (Q)^t \overline{\Delta d}} \tag{A8}$$

(c) $\frac{\partial \mathcal{L}}{\partial \sigma} = \mathbf{0}$

$$\begin{aligned}\frac{\partial \mathcal{L}}{\partial \sigma} &= -\partial_\sigma < \lambda_\sigma, C(\sigma) - m > -\partial_\sigma < \lambda_e, A(\sigma)E^S - b^s > \\ 0 &= -\partial_\sigma C(\sigma)^\dagger \lambda_\sigma - \left[\partial_\sigma (A(\sigma)E^S)^\dagger - \partial_\sigma b^\dagger)\right] \lambda_e \\ \lambda_\sigma &= -(\partial_\sigma C(\sigma)^\dagger)^{-1} \left[\partial_\sigma (A(\sigma)E^S)^\dagger - \partial_\sigma b^\dagger)\right] \lambda_e \end{aligned} \tag{A9}$$

If no grid transformation a parametrization of m equal to the conductivity medium σ as stated in the forward problem as :

$$m = C(\sigma) = \sigma \tag{A10}$$

A relation between λ_σ and the adjoint field λ_e is obtained in the last adjoint state function:

$$\boxed{\lambda_\sigma = -\left[\partial_\sigma (A(\sigma)E^S)^\dagger - \partial_\sigma b^\dagger)\right] \lambda_e} \tag{A11}$$

(iii)The third step is to evaluate the gradient, which correspond to the derivative of $\mathcal{L}$ with respect to m considering each state variable independent of m (comprising d^{cal} in the cost function):

$$\begin{aligned}\frac{\partial \mathcal{L}}{\partial m} &= -\partial_m < \lambda_\sigma, C(\sigma) - m > \\ \frac{\partial \mathcal{L}}{\partial m} &= \lambda_\sigma \end{aligned} \tag{A12}$$

The gradient is therefore obtained with respect to the adjoint variable λ_σ for which the expression was determined in eq. (A11):

$$\boxed{\partial_m \chi = \lambda_\sigma} \tag{A13}$$

Gradient solution

The adjoint field solution λ_e obtained through the solution of the linear system $Ax = b$ (eq. A8), the gradient can be computed with:

$$\partial_m \chi = \lambda_\sigma = -(\partial_\sigma C(\sigma)^t)^{-1} \left[\partial_\sigma (A(\sigma)E^S)^\dagger - \partial_\sigma b^\dagger)\right] \lambda_e \tag{A14}$$

(i) Derivation of A matrix and the source term by σ results in:

$$\partial_\sigma (A(\sigma)E^S)^\dagger = (i\omega\mu)^\dagger E^{S\dagger} \tag{A15}$$

(ii) and for the source term:

$$\partial_\sigma b^* = (-i\omega\mu)^* E^{P*} \tag{A16}$$

The gradient of the objective function is then obtained for a real conductivity parametrization ($m = \sigma^r$) with:

$$\boxed{\partial_m \chi = -\left[i\omega\mu E^{\text{tot}}\right]^\dagger \lambda_e} \tag{A17}$$

APPENDIX B: ERROR ESTIMATION

Error estimation on the result of the inversion was calculated using a weighted root mean square deviation:

$$rms = \sqrt{\frac{(\Delta d W_d)^\dagger W_d \Delta d}{N_d}} \tag{B1}$$

vector W_d is defined as the inverse of the data standard deviation. For synthetic data, standard deviation is defined according to a relative error e:

$$W_d^{\text{linear}} = 1/\sigma \qquad \text{with } \sigma \text{ the standard deviation} \tag{B2}$$

$$W_d^{\text{linear}} = \frac{1}{|d_{\text{obs}}|e} \qquad \text{with e the relative error} \tag{B3}$$

As we are using the logarithm of the data (logarithm of the amplitude of the considered EM field and its phase) the standard deviation had to be converted for its log equivalent. The variance and standard deviation of an observed data in logarithm can be written according to its relative error as:

$$\begin{aligned}\sigma_{\log}^2 &= (\log(d_{\text{obs}} + e d_{\text{obs}}) - \log(d_{\text{obs}}))^2 \\ \sigma_{\log}^2 &= \log\left(\frac{d_{\text{obs}} + e d_{\text{obs}}}{d_{\text{obs}}}\right)^2 \\ \sigma_{\log} &= \log(1 + e) \end{aligned} \tag{B4}$$

A relation independent of the magnitude of the data is obtained. The covariance matrix for logarithmic data is thus written as:

$$W_d^{\log} = \frac{1}{\log(1+e)} \simeq \frac{1}{e} \qquad \text{for small variation} \tag{B5}$$

By using a relative error representing 1 per cent of the total field amplitude for rms computation, the weighted rms can be seen as a percentage of variation of the data fit. Relative error are thus estimated for a component of the field E^k (k, being the X or Y component of the field) in comparison to the total field E_{tot} then $e_{1\text{ per cent}} = \frac{0.01|E^{\text{tot}}|}{|E^k|}$. $e_{1\text{ per cent}}$ is then the value used in eq. (B4) for covariance computation.